The Sensitivity of an Idealized Weddell Gyre to Horizontal Resolution

Andrew F. Styles[1] , Michael J. Bell[2] , and David P. Marshall[1]

[1]Department of Physics, University of Oxford, Oxford, UK, [2]Met Office, Exeter, UK

Abstract Estimates of the Weddell Gyre transport vary widely between climate simulations. Here, we investigate if inter-model variability can originate from differences in the horizontal resolution of the ocean model. We run an idealized model of the Weddell Gyre at eddy-parameterized, eddy-permitting, and eddy-rich resolutions and find that the gyre is strongly sensitive to horizontal resolution. The gyre transport is largest at eddy-permitting resolutions (45 Sv with a noisy bathymetry) and smallest at eddy-parameterized resolutions (12 Sv). The eddy-permitting simulations have the largest horizontal density gradients and the weakest stratification over the gyre basin. The large horizontal density gradients induce a significant thermal wind transport and increase the mean available potential energy for mesoscale eddies. The distribution of eddy kinetic energy indicates that explicit eddies in simulations intensify the bottom circulation of the gyre via non-linear dynamics. If climate models adopt horizontal resolutions that the Weddell Gyre is most sensitive to, then simulations of the Weddell Gyre could become more disparate.

Plain Language Summary The Weddell Gyre is a large horizontal circulation in the southern hemisphere. The gyre is exposed to low atmospheric temperatures and lies under extensive sea ice. Extremely dense water forms in the Weddell Sea, which the Weddell Gyre exports to the global ocean. These exported dense water masses change the Earth's climate by altering the total heat and carbon content in the global ocean. Between climate simulations, the volume of water transported by the Weddell Gyre varies significantly: we investigate if this variability can originate from differences in the horizontal spatial resolution of the ocean models. Using a simplified model of the Weddell Gyre, we find that the intensity of the circulation is extremely sensitive to the horizontal resolution. The circulation is particularly strong at intermediate resolutions, where only the largest ocean eddies are resolved. At intermediate resolutions, horizontal density gradients are the largest and the vertical density gradients are the smallest; this unique density structure allows for a particularly strong Weddell Gyre circulation. These results have important implications for long-range ocean climate projections.

1. Introduction

The Weddell Gyre is the largest subpolar gyre in the southern hemisphere and spans an area of approximately 6 million square kilometers in the Atlantic sector of the Southern Ocean (Vernet et al., 2019). Buoyancy forcing in this region is intense as atmospheric temperatures are low and sea ice formation is extensive. The sea ice insulates the ocean from the cold atmosphere but offshore winds can sustain coastal polynyas which enable strong buoyancy forcing through brine rejection (Abernathey et al., 2016; Haid & Timmermann, 2013). The Weddell Gyre also lies immediately south of the Antarctic Circumpolar Current (ACC), the strongest current in the global ocean.

Extremely dense water masses are produced in the Weddell Gyre as small bodies of water are exposed to intense buoyancy forcing for a prolonged period of time. Of particular interest is the production and export of Antarctic Bottom Water (AABW), which contributes to the southern closure of the global overturning circulation when exported northwards (Lumpkin & Speer, 2007; J. Marshall & Speer, 2012; Sloyan & Rintoul, 2001; Talley et al., 2003). The Weddell Gyre strength can control the variability of dense water export (Meijers et al., 2016) and could potentially influence global overturning. There is some debate about how much AABW is produced and exported by the Weddell Gyre and a review can be found in Vernet et al. (2019).

The surrounding coastline and local topographic features shape the Weddell Gyre, as seen in Figure 1a. The southern limb of the gyre follows the border of the Antarctic mainland and the western limb is steered north by the Antarctic Peninsula. The eastern boundary of the Weddell Gyre is a dynamic feature and it is uncertain whether
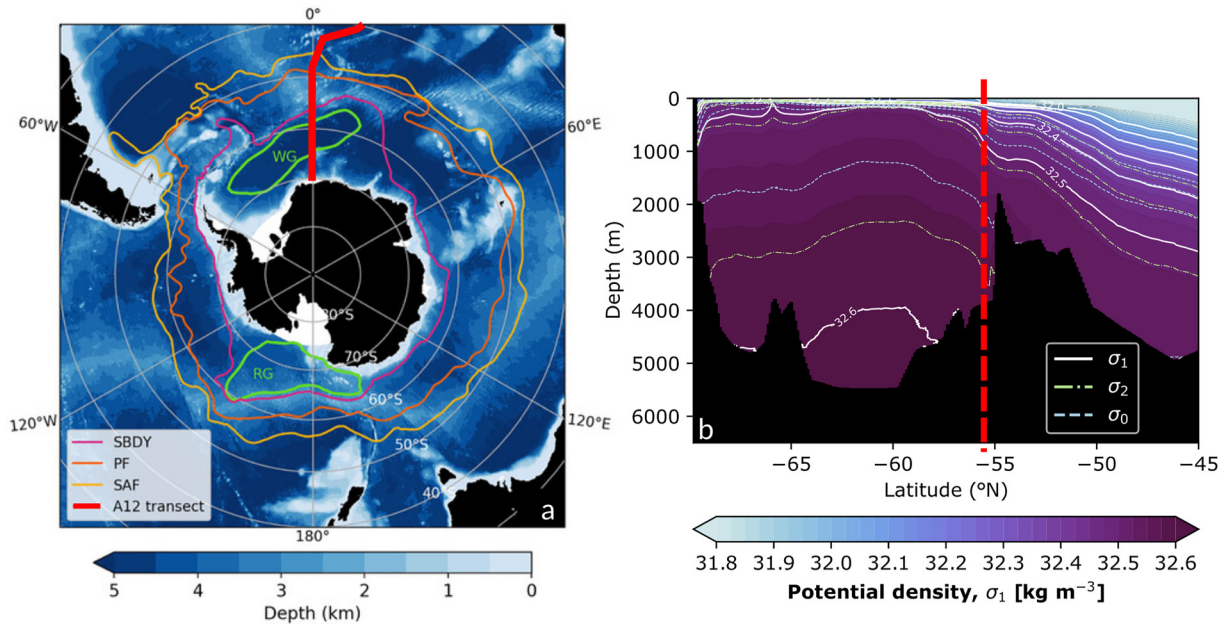
Figure 1. Bathymetric and hydrographic features of the Southern Ocean. (a) From Wilson et al. (2022), the bathymetry of the Southern Ocean. The contours mark three fronts of the Antarctic Circumpolar Current (ACC) (Orsi et al., 1995): Southern Boundary (SBDY), Polar Front (PF), and Subantarctic Front (SAF). Outlines of the Weddell Gyre and Ross Gyre (RG) are also shown, using contours of satellite-based dynamic ocean topography (Armitage et al., 2018). (b) Potential density along the A12 transect (red line in (a)) calculated using conservative temperature and absolute salinity measurements from 10 hydrographic sections. The gridded hydrographic data originates from the GO-SHIP Easy Ocean product (Katsumata et al., 2022). White contours show potential density surfaces that are calculated with a reference pressure of 1,000 dbar (σ_1). Green and blue contours show similar potential density surfaces that are calculated with a reference pressure of 2,000 (σ_2) and 0 (σ_0) dbar respectively.

any topographic feature limits it. Estimates of the eastern boundary location range from 30°E (Deacon, 1979) to as far as 70°E (Park et al., 2001). Within this longitudinal range there is an abundance of eddies that allow exchange between the gyre and ACC (Park et al., 2001; Ryan et al., 2016; Schröder & Fahrbach, 1999).

Two zonally-elongated ridges act as partial barriers between the ACC and Weddell Gyre: the South Scotia Ridge in the west and the North Weddell Ridge in the east (Vernet et al., 2019). These ridge systems are typically within 1,500 to 2,000 m of the sea surface. Submarine ridges block deep currents from crossing the ACC-gyre interface and play a major role in setting the stratification across the entire region (Orsi et al., 1993; Wilson et al., 2022). Figure 1b illustrates the potential density based on hydrographic sections of the Weddell Gyre and ACC. The contours of potential density in the Weddell Gyre are domed and there is a steep meridional density gradient above the submarine ridge (approx. 54°S in Figure 1b). As seen in Figure 1b, this is true if a reference pressure of 0 (σ_0), 1000 (σ_1), or 2000 (σ_2) dbar is used when calculating the potential density. As a result, only the densest components of the circumpolar flow are exposed to the intense buoyancy forcing found near the sea surface of the Weddell basin and on the continental shelf (Naveira Garabato et al., 2016).

Measurements of the Weddell Gyre transport are limited and vary widely. Gordon et al. (1981) use wind stress data and apply Sverdrup balance to estimate the Weddell Gyre transport as 76 Sv (1 Sv = 10^6 m^3 s^{-1}) while questioning the validity of Sverdrup dynamics. Moorings and ship data provide lower estimates of the transport, for example, 20–56 Sv from Fahrbach et al. (1991) and 30 Sv from Yaremchuk et al. (1998). In Reeve et al. (2019), the Weddell Gyre transport is estimated to be 32 ± 5 Sv using Argo data (Argo, 2020). Although recent Argo data have significantly increased the number of available observations, coverage is still fairly limited within the Weddell Gyre. Argo data has contributed approximately 28,000 hydrographic profiles (south of 60°S) over a time period of 14 years with no measurements taken below 2,000 dbar. Reeve et al. (2019) use the thermal wind relation to estimate the geostrophic velocity in the upper 2,000 dbar of the Weddell Gyre and extrapolate over depth to estimate the full volume transport while relying on ship-based observations to estimate the extrapolation error.

Climate models disagree on the strength and shape of the Weddell Gyre and limited winter-time observations make it difficult to assess model accuracy in this region. Wang (2013) studies 14 climate simulations from Phase

5 of the Coupled Model Intercomparison Project (CMIP5) with horizontal grid spacings of 1° or larger and finds that the time-averaged Weddell Gyre transport ranges from approximately 10 to 80 Sv. This is troubling as Meijers et al. (2016) suggest that variability in the export of dense Weddell Sea slope water is closely tied to wind-driven acceleration of the Weddell Gyre's western boundary current. Inconsistent Weddell Gyre circulations between climate models may lead to inconsistent descriptions of the global overturning circulation and consequently inconsistent global heat, carbon, and freshwater budgets. In the South Scotia Ridge, there are deep passages that are important AABW export pathways. These pathways cannot be resolved in 1° models but will be present in future generations of climate models with a finer horizontal resolution. It is therefore possible that future climate models will be more sensitive to the Weddell Gyre transport than they are now.

Long time integrations of numerical ocean models under different climate forcing scenarios are prohibitively expensive to run at mesoscale eddy-resolving resolutions, but high resolution simulations are becoming increasingly affordable. Hewitt et al. (2020) comment that the average horizontal resolution of the ocean has increased with each iteration of the Coupled Model Intercomparison Project (CMIP) and this corresponds to an approximate doubling of horizontal resolution every 10 years (Fox-Kemper, 2018). The majority of centers participating in Phase 6 of CMIP (CMIP6) parameterize the effect of unresolved eddies, but there are now several "eddy-permitting" models that at least partially resolve the mesoscale eddies (Hewitt et al., 2020), taking into account the small Rossby deformation radius at these high latitudes (Hallberg, 2013).

Significantly more observations are needed to assess how mesoscale eddies influence the Weddell Gyre transport in the real ocean and there are not enough eddy-permitting climate simulations in CMIP6 to accurately assess how explicit eddies influence the Weddell Gyre in climate projections. When studying the role of mesoscale eddies in the Weddell Gyre, a hierarchy of models with different resolutions can be a powerful tool. In Adcroft et al. (2019), the results of a 0.5° and a 0.25° ocean-ice model (GFDL OM4.0) are compared. These two models only differ in resolution and physical parameterization and produce similar density structures in the Weddell Sea at 42°W. Neme et al. (2021) study the Weddell Gyre more directly in another hierarchy of ocean-ice models, ACCESS-OM2 (Kiss et al., 2020), and find that the time-averaged Weddell Gyre transport increases from 34 to 41 Sv when the horizontal grid spacing is reduced from 1° to 0.1°. Models such as those studied by Adcroft et al. (2019) and Neme et al. (2021) offer realism but are less configurable and more computationally expensive than idealized models that might demonstrate similar behavior.

In the idealized and eddy-permitting simulations by Wilson et al. (2022), the introduction of a zonal submarine ridge intensifies the Weddell Gyre. Wilson et al. (2022) also comment that the ACC and Weddell Gyre primarily interact through transient eddies on the eastern boundary of the zonal ridge. In this article, we aim to investigate how mesoscale eddies can influence the Weddell Gyre and its interaction with the ACC. We do this by varying the horizontal resolution of an idealized model over a wide range of horizontal grid spacings including: eddy-parameterized scales (80 and 40 km), eddy-permitting scales (10 and 20 km), and eddy-rich scales (3 km). The Weddell Gyre is found to be extremely sensitive to horizontal resolution and is strongest at eddy-permitting resolutions.

The article is structured as follows. In Section 2 we describe the idealized model used in this study and in Section 3 we describe the three experiments that are carried out. In Section 4 we present our results including a thermal wind decomposition of the Weddell Gyre and ACC transport. In Section 5, we discuss how mesoscale eddies can strengthen the flow at the sea floor and the missing physics in our model design. Closing remarks are made in Section 6.

2. Model Design

The experiments presented in this article are performed in the NEMO Community Ocean model (Madec et al., 2019). NEMO has been used for several idealized gyre studies (Lévy et al., 2010, 2015; Perezhogin, 2019; Ruggiero et al., 2015; Styles et al., 2022) and the presented configuration is similar to the model used by Wilson et al. (2022). The configuration features a zonally periodic channel and a southern continental shelf which resembles the neighboring coastline for the Weddell Gyre (see Figure 2a). Two large landmasses are present on the western margins of the model, with an opening that crudely represents the Drake Passage. Additional topographic features include a submarine ridge which extends eastwards from the idealized Drake Passage and a meridional sill in the Drake Passage that blocks f/H contours and regulates the ACC transport (f is the Coriolis parameter and
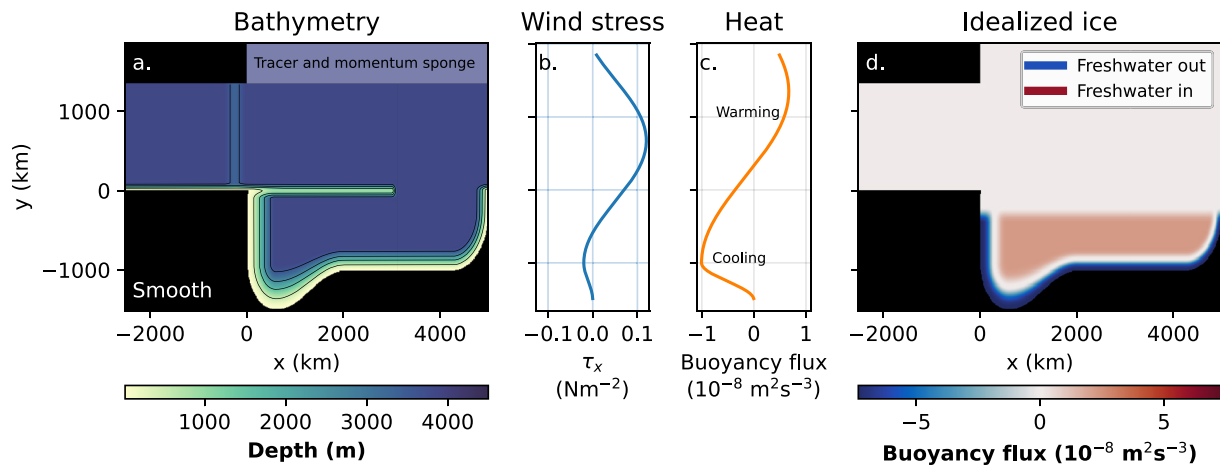
Figure 2. Summary of the model configuration. (a) Bathymetry of the model (without topographic noise) with contours at 1,000 m intervals. (b) The zonal wind stress profile for the configuration. (c) The zonal heat flux profile for the configuration in units of buoyancy flux. (d) The freshwater fluxes used to represent sea ice for the configuration in units of buoyancy flux. In this model, a buoyancy flux of 10^{-8} m² s⁻³ corresponds to 14.9 W m⁻² of surface heating or approximately 4×10^{-5} kg m⁻² s⁻¹ of freshwater input (assuming a surface salinity of 35 psu).

H is the ocean depth). The parameters for these topographic features and all other relevant fixed parameters can be found in Table 1. Throughout this article, the x coordinate is the zonal displacement from the eastern boundary of the Drake Passage and the y coordinate is the meridional displacement from the southern boundary of the Drake Passage (see axes in Figure 2a).

The model has a regular horizontal grid with a horizontal grid spacing between 80 and 3 km, depending on the experiment (see Table 2). For context, on the "ORCA" family of grids (Madec & Imbard, 1996) at 65°S the horizontal grid spacing is around 50 km in a 1° model, 12 km in a 0.25° model, and 5 km in a 0.1° model. All configurations use z-coordinates and have 31 vertical model levels, with vertical spacing that is approximately 10 m near the sea surface, 315 m near the sea floor, and partial cells are used to represent the varying sea floor. By only varying the horizontal resolution, we are only exploring dynamics that do not require higher order vertical modes. The configuration exists on a beta plane where the Coriolis parameter varies linearly with the meridional coordinate, y, around its value at 65°S ($y = 0$ in Figure 2). The model uses a free slip condition on lateral boundaries and applies a linear friction to the bottom boundary with a linear friction coefficient of 4×10^{-4} m s⁻¹. A simplified linear equation of state is used with a thermal expansion coefficient of $a_0 = 2.8 \times 10^{-4}$ kg m⁻³ K⁻¹ and a haline coefficient of $b_0 = 7.7 \times 10^{-4}$ kg m⁻³ psu⁻¹. When using a linear equation of state, there is no distinction between conservative and potential temperature, nor is there a distinction between absolute and practical salinity; therefore, in our results we will simply refer to temperature and salinity. The horizontal diffusion of momentum and tracers is implemented with a diffusivity that scales linearly with horizontal grid spacing (see Table 1). Subgrid scale vertical mixing of momentum and tracers is represented by the Turbulent Kinetic Energy scheme (Bougeault & Lacarrere, 1989; Gaspar et al., 1990).

The model is forced with a sinusoidal and zonal wind stress which only varies in the meridional direction. The wind stress profile resembles the zonally and annually averaged wind stress across the Southern Ocean (Figure 2b), with a maximum westerly wind stress of 0.12 N m⁻² over the center of the circumpolar channel and a peak easterly wind stress of 0.02 N m⁻² along the continental shelf. Similarly, the surface heat flux is also sinusoidal and

Table 1
Summary of Fixed Parameters in the Model

Model parameter	Value
Meridional domain size	3,350 km
Zonal domain size	7,520 km
Reference Coriolis parameter	-1.3×10^{-4} s⁻¹
Meridional gradient of Coriolis parameter	9.6×10^{-12} m⁻¹ s⁻¹
Momentum diffusivity (resolution dependent)	$(0.05 \, \Delta x)$ m² s⁻¹
Tracer diffusivity (resolution dependent)	$(0.005 \, \Delta x)$ m² s⁻¹
Maximum (smooth) ocean depth	4,000 m
Number of model levels	31
Vertical resolution	10–315 m
Continental shelf width	300–600 km
Drake Passage zonal length	2,520 km
Drake Passage meridional width	1,350 km
Drake passage sill zonal width	500 km
Drake passage sill maximum height[a]	500 m
Submarine ridge zonal extent	3,000 km
Submarine ridge meridional width	200 km
Submarine ridge maximum height	3,000 m
Root mean square of topographic noise	100 m
Topographic noise length scales	240, 120, 60, 30, 9 km
Topographic noise relative amplitudes	8, 4, 2, 1, 0.3

Note. Δx is the horizontal grid spacing of the model in meters.

[a]The sill height is varied for the ACC sensitivity experiment but is 500 m for all other experiments.

Table 2
Summary of the Numerical Experiments

Experiment series	Horizontal grid spacing (km)					Topographic noise
	80[GM]	40[GM]	20	10	3	
Smooth	✓	✓	✓	✓	✗	✗
Rough	✓	✓	✓	✓	✓	✓
ACC sensitivity (11 variations of sill height)	✓	✓	✓	✓	✗	✓

Note. Experiments marked with GM use the Gent and McWilliams (1990) eddy parameterization. In total 44 ACC sensitivity experiments were conducted (11 for each horizontal grid spacing between 80 and 10 km).

zonally uniform with a maximum surface warming of 10 W m^{-2} at the northern boundary of the Drake Passage and a peak cooling of 15 W m^{-2} on the south continental shelf. The surface heat flux is shown in units of buoyancy flux in Figure 2c.

The effect of sea ice on the salinity budget is simply represented by a surface freshwater flux, as shown in units of buoyancy flux in Figure 2d. The freshwater fluxes resemble the annual-average freshwater fluxes due to sea ice in the Southern Ocean, with net freshwater release in the Weddell basin and persistent sea ice formation on the southern continental shelf (Pellichero et al., 2018). Freshwater fluxes are the dominant buoyancy flux in the Weddell basin, as argued by Pellichero et al. (2018), but they do not extend onto the submarine ridge in the idealized model. The domain area integral of freshwater fluxes is identically zero to conserve the water content of the model. The model was also tested without the idealized sea ice. Removing the idealized sea ice does not change the gyre or ACC's sensitivity to resolution but the isopycnals are less realistic above the continental shelf.

The northern margin of the model ($y > 1,350$ km) contains a sponge layer, which parameterizes the effect of the global ocean to the north. The horizontal flow is relaxed to rest, the salinity is relaxed to 35 psu at all depths, and the temperature is relaxed to the vertical profile,

$$T(z) = T_{\text{top}} \exp(z/\delta_z), \tag{1}$$

where T is the temperature, z is the vertical coordinate, $T_{\text{top}} = 10°C$ is the prescribed sea surface temperature and $\delta_z = 1,500$ m is the decay length scale of the surface temperature. Consequently, the prescribed sea floor temperature is approximately 0°C. The momentum sponge has a maximum relaxation timescale of approximately 10 days and the tracer sponge has a maximum relaxation timescale of approximately 100 days. The sponge layer is 500 km wide and the relaxation timescale varies with y sinusoidally, increasing from zero to the maximum value.

The model's initial state features a sinusoidal ACC with a peak zonal velocity of 0.2 m s^{-1} in the channel center and a zero velocity at $y = 0$ km and $y = 1,350$ km. The ACC velocity profile decays with depth similarly to the temperature in the northern sponge (Equation 1). The initial state of the gyre basin (south of $y = 0$) is at rest. The initial temperature profile is calculated using the thermal wind relation, integrating south from the northern sponge where the temperature profile matches Equation 1. Similarly to the sponge layer, the initial salinity is 35 psu everywhere in the domain.

In some experiments (see the next section) topographic noise is introduced to the bathymetry, as shown in Figure 3. The addition of weak topographic noise permits topographic interactions everywhere in the domain but only perturbs the larger scale bathymetric features. The analytic noise field is generated using a zonally periodic and continuous noise generation function, $\mathcal{N}(x, y)$, from OpenSimplex (Spencer, 2022). Noise is added at various length scales as shown below,

$$\lambda(x, y) \propto \sum_{i=1}^{N_L} \mathcal{N}\left(\frac{x}{L_i}, \frac{y}{L_i}\right) L_i, \tag{2}$$

where λ is the final two dimensional noise function, L_i is the ith length scale used (listed in Table 1), and N_L is the number of length scales used. The continuous function, $\lambda(x, y)$, is then evaluated on the grid used for each experiment and scaled so that the root mean square (rms) of the discrete noise field is 100 m in all configurations. Each length scale introduces a topographic gradient with a magnitude that is independent of L_i, as demonstrated below,

$$\nabla\lambda(x, y) \propto \sum_{i=1}^{N_L} \nabla\mathcal{N}\left(\frac{x}{L_i}, \frac{y}{L_i}\right). \tag{3}$$
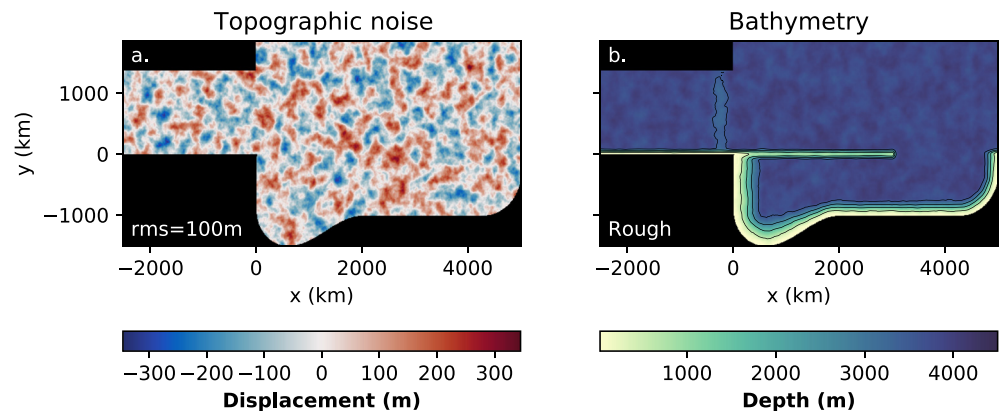
Figure 3. (a) Noise profile and (b) bathymetry for the Rough simulation with a horizontal grid spacing of 3 km. All discrete noise fields used in this article have a root mean square of 100 m and are based on the same continuous noise function, $\mathcal{N}(x, y)$.

As seen in Figure 3, the maximum displacement caused by the noise field is approximately 300 m and the structure of the continental shelf and other large topographic features is not lost to the noise. In cases where the added noise would create islands in the domain, the noise is locally reduced to keep all topographic features submerged.

In Section 5, we will discuss the important differences between this idealized configuration and the real ocean and assess how the discrepancies may modify the results presented in this article.

3. Experimental Setup

The model described in the previous section is computationally affordable and a wide parameter space can be explored. In total, 78 simulations were conducted with a minimum run time of 220 years. A summary of the experiments is shown in Table 2 and the computational cost is summarized in Appendix A. There are three sets of experiments: Smooth, Rough, and ACC sensitivity. The Smooth experimental series uses the bathymetry shown in Figure 2a and does not feature any topographic noise. The horizontal grid spacing is varied from 80 to 10 km and only the 80 and 40 km simulations include the Gent and McWilliams (1990) eddy parameterization (GM hereafter). The 80 and 40 km simulations use a constant GM diffusivity parameter of 2,000 m² s⁻¹. The Rough series is exactly the same as the Smooth series but uses topographic noise, as shown in Figure 3, and the horizontal grid spacing varies from 80 to 3 km. The 3 km simulation is eddy-rich and computationally expensive so only one eddy-rich time integration could be completed. In Section 4.5, we also test various applications of GM on eddy-permitting and eddy-parameterized simulations to see how this affects our main results.

In this model the ACC is driven by wind-stress, surface buoyancy forces, and buoyancy forcing on the northern boundary. The ACC transport is not prescribed, so the ACC strength is free to respond to changes in the horizontal resolution. The ACC sensitivity experiment series is designed to assess how strongly the Weddell Gyre and ACC transports are coupled. Not only is a study of the gyre-ACC coupling scientifically interesting; it is also necessary to assess if the changes in the Weddell Gyre transport with resolution are influenced by changes in the idealized ACC strength. In the ACC sensitivity experiments, the height of the Drake Passage sill is varied from 500 m to 2,500 m in intervals of 200 m: this modifies the strength of the simulated ACC in a way that does not modify the immediate conditions for the Weddell Gyre. For example, we cannot modify the wind stress to change the ACC strength as this will alter the wind stress curl above the gyre and change the gyre strength directly. Modifying the wind stress would also be further complicated by eddy saturation effects in simulations with explicit eddies (D. P. Marshall et al., 2017).

4. Results

As seen in Figure 4, 200 years is a sufficient spin up time to assume a statistically steady Weddell Gyre and ACC transport. The transports in Figure 4 are calculated from annual averages of the depth-integrated stream function. The ACC transport is the zonal average of the stream function along the northern boundary of the domain and the Weddell Gyre transport is the maximum value of the stream function in the gyre basin (south of $y = 0$). Only the gyre transport in the 3 km simulation shows a slight downward trend that does not alter the interpretation of the presented results. We also find that the spatial average of temperature and salinity are also statistically
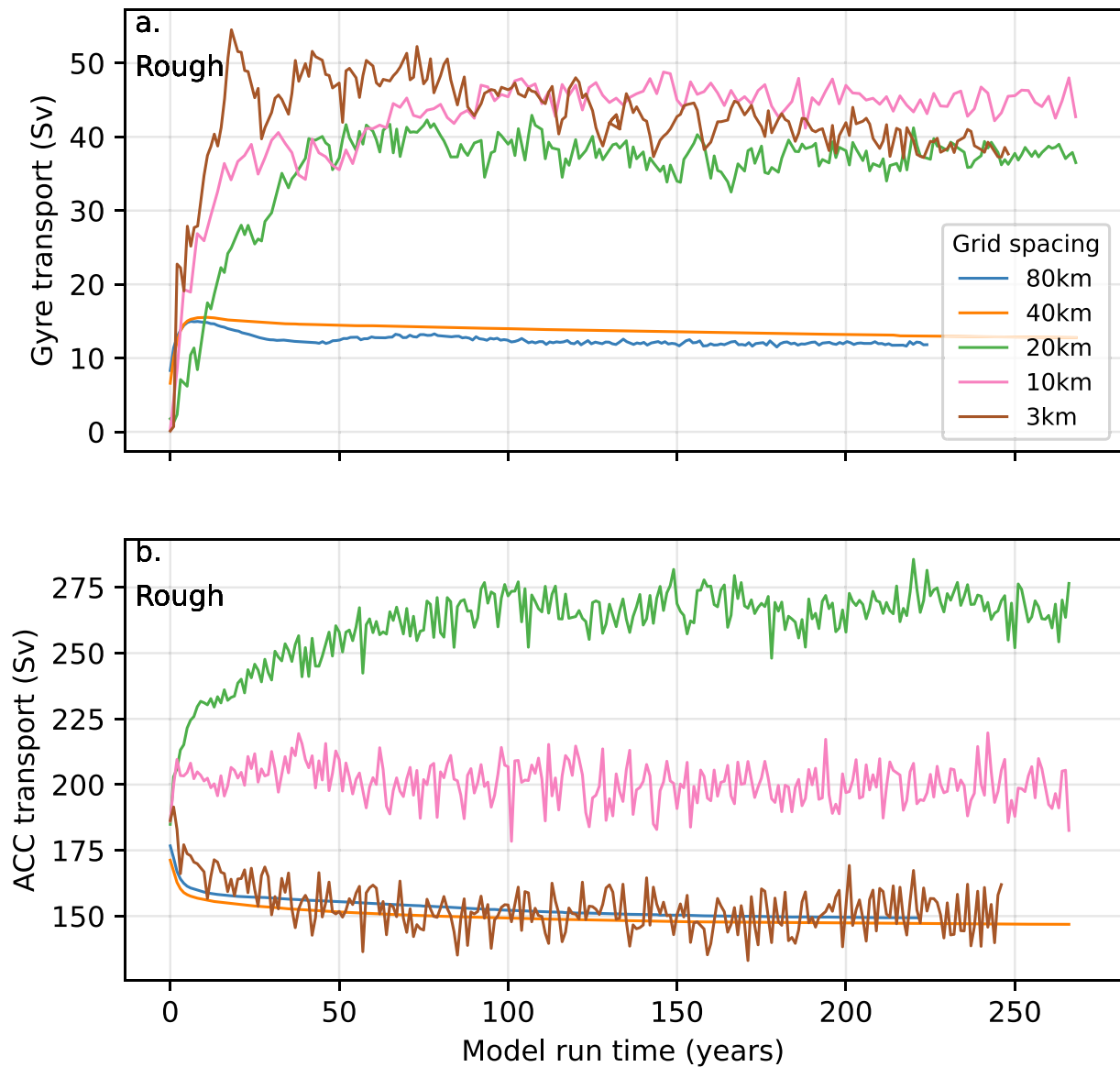
Figure 4. Evolution of the (a) Weddell Gyre and (b) Antarctic Circumpolar Current transports for configurations with rough bathymetry.

steady. Figure 5 shows the evolution of the domain-averaged temperature and salinity for configurations with a rough bathymetry. All configurations have statistically-steady temperature and salinity but the eddy-permitting configurations are on average 0.2–0.4°C cooler than the eddy-parameterized and eddy-rich simulations.

All results presented in this section are time-averages taken from the final 20 years of each model run. As indicated by Figure 6, the 3 km simulation resolves a rich eddy field in the ACC and near the eastern boundary of the zonal ridge. Similar to Wilson et al. (2022), a weaker but qualitatively similar eddy field is partially resolved in 10 and 20 km simulations. The distribution of eddy kinetic energy is discussed further in Section 5.1.

4.1. Transport Sensitivity to Resolution

In the Rough and Smooth configurations, the Weddell Gyre and ACC are strongly sensitive to resolution, as shown in Figure 7. The transports are calculated from the 20 year time-average of the depth-integrated stream function. Figure 7a shows how the Weddell Gyre transport increases as the resolution is doubled over smooth bathymetry. The time-averaged Weddell Gyre transport is 28.9 Sv in the 80 km simulation and increases to 54.7 Sv in the 10 km simulation. Introducing a rough bathymetry reduces all gyre transports (17 Sv reduction for
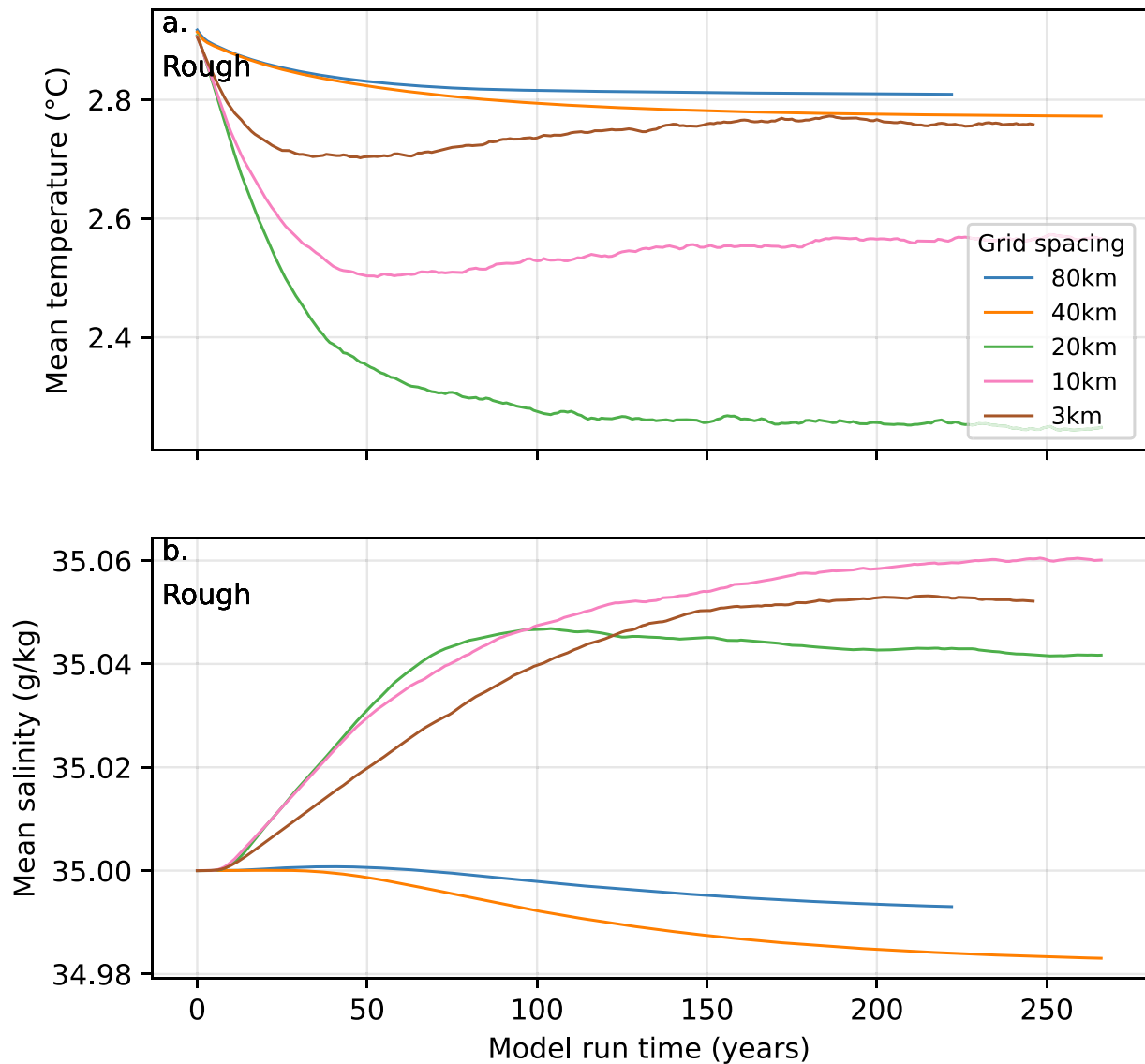
Figure 5. Evolution of the domain-averaged (a) temperature and (b) salinity for configurations with rough bathymetry.

the 80 km case, 10 Sv reduction for the 10 km case) but also increases the Weddell Gyre's sensitivity to resolution (Figure 7c). With a rough bathymetry, the time-averaged Weddell Gyre transport is 11.9 Sv in the 80 km configuration and then rapidly increases to 44.8 Sv in the 10 km configuration. For the Rough configuration, we have access to an eddy-rich simulation where the Weddell Gyre transport is 38.6 Sv. In this case, the transition from an eddy-permitting to an eddy-rich simulation reduces the Weddell Gyre transport by 6.2 Sv. The red error bars in Figures 7a–7d show the interannual variability of the gyre and ACC transports during the experimental period (two standard deviations either side of the average). The limited overlap of adjacent error bars suggests that the gyre and ACC transports for almost any year in our experiment are similar to the time-averaged results.

In Figure 7, the time-averaged stream function for the gyre shrinks and follows the bathymetry more closely when the resolution increases from eddy-parameterized (80 km) to eddy-permitting (10 km) scales. The boundary current that forms on the submarine ridge becomes particularly narrow and intense. In Section 4.3 we use a thermal wind decomposition to relate the transports and stream functions shown in Figure 7 to horizontal density gradients and the velocity at the sea floor.

The structure of the ACC is sensitive to the coarseness of the bathymetry. In the Smooth configurations, the ACC is deflected northwards by the ridge in the Drake Passage but quickly returns to a zonal flow which results in large
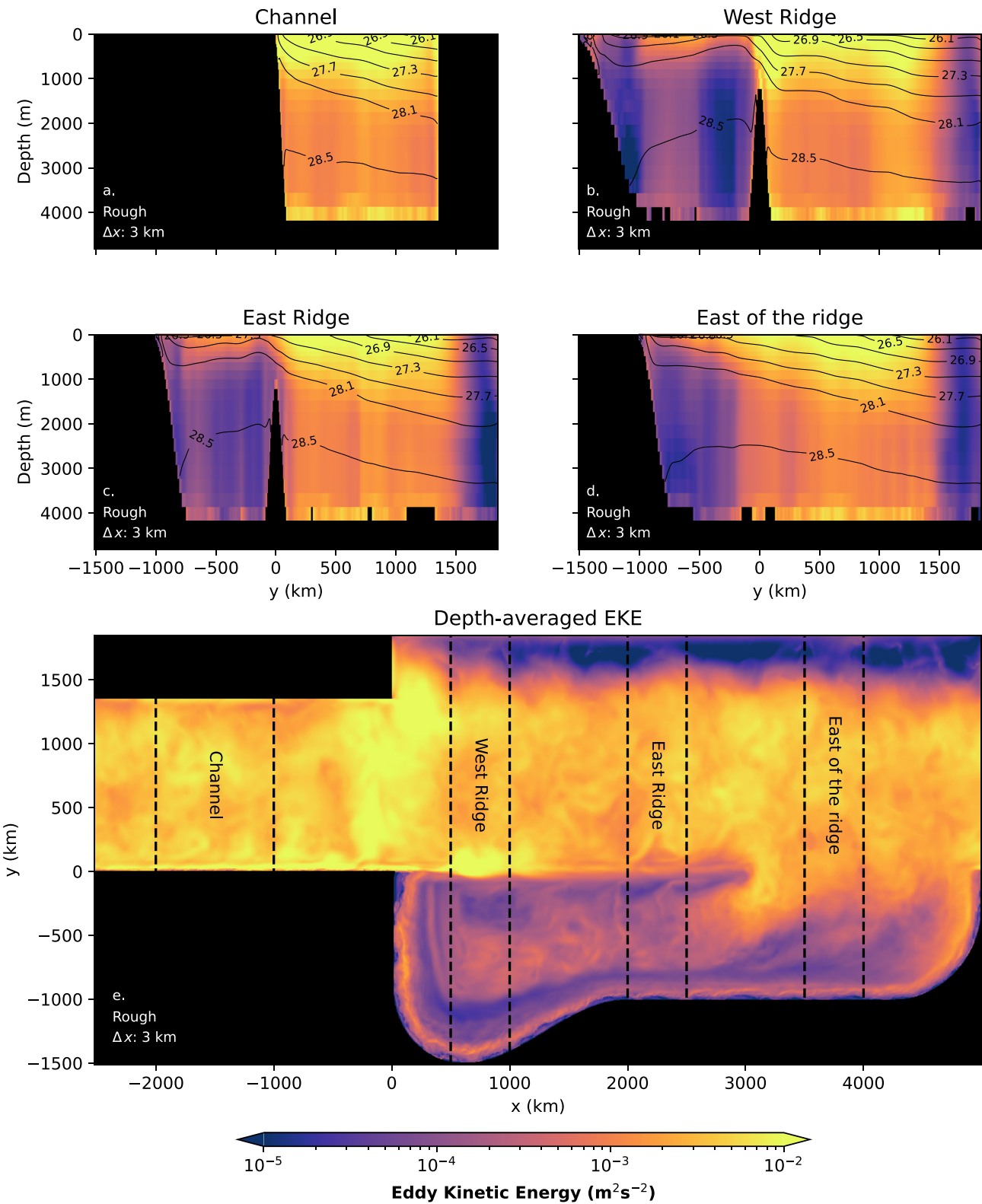
Figure 6. (a–d) Zonal averages and the (e) depth average of the eddy kinetic energy in a simulation with a 3 km horizontal grid spacing and rough bathymetry. The zonal averages in (a)–(d) are taken over various meridional sections that are shown in (e). The black contours in (a)–(d) show the zonally-averaged density surfaces across the meridional section.
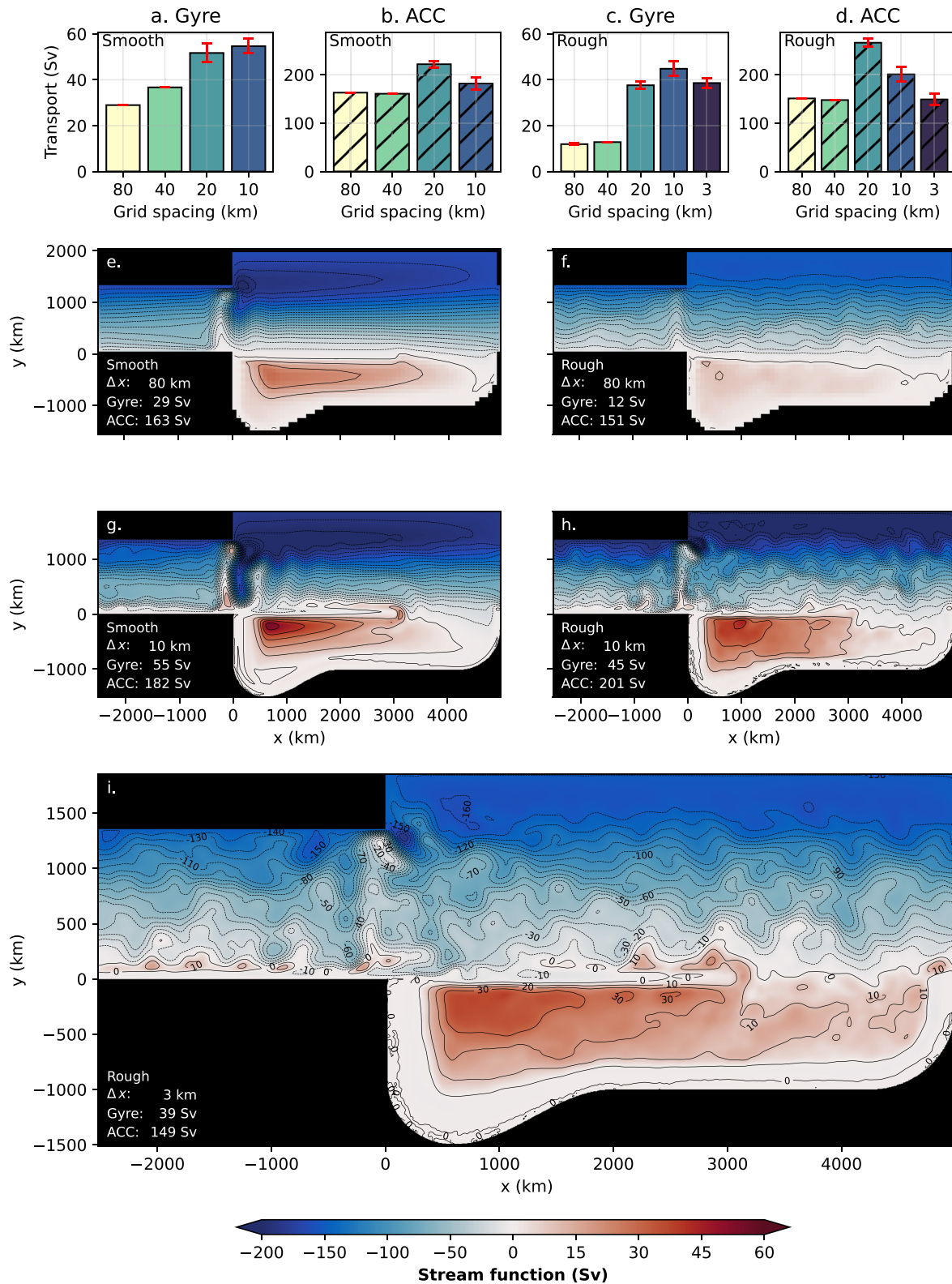
Figure 7. Sensitivity of the Weddell Gyre and Antarctic Circumpolar Current (ACC) transport to resolution. (a)–(d) Show the time-averaged gyre and ACC transport over smooth and rough bathymetry. Red error bars show the inter-annual variability of the transport (two standard deviations). (e)–(i) Are the time-averaged stream functions from configurations at an eddy-parameterized resolution (80 km), an eddy-permitting resolution (10 km), and an eddy-rich resolution (3 km). The black contours have an interval of 10 Sv.
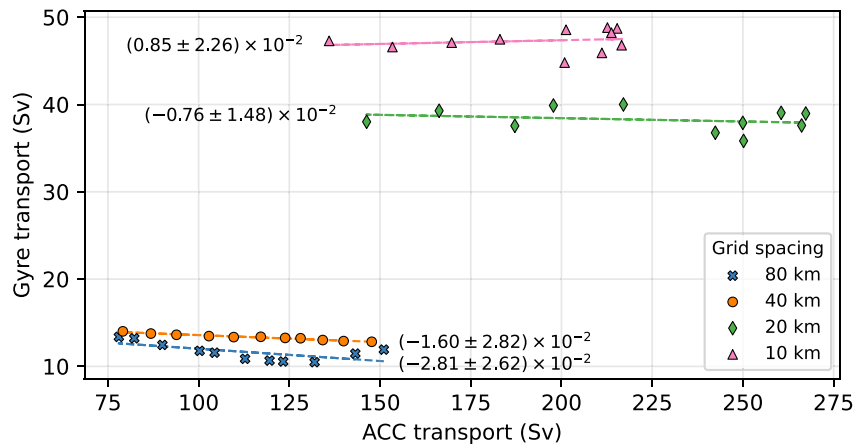
Figure 8. How the Weddell Gyre transport varies with respect to the Antarctic Circumpolar Current (ACC) transport at several resolutions. The dashed line shows the straight line of best fit which is calculated using a least squares method. The value of the slope (dimensionless) and error is provided for each line. The gyre transport is insensitive to large variations in the ACC transport.

positive and negative meridional velocities in the ACC (Figure 7g). In the Rough configurations, the northward deflection of the ACC is similarly severe but the topographic noise appears to dampen the ACC's return to a zonal flow (Figures 7h and 7i). The ACC's behavior in the Rough configurations more closely resembles the ACC's abrupt equatorward deflection east of the Drake Passage and the current's more steady poleward trajectory while circumnavigating Antarctica (see Figure 7 of Mazloff et al. (2010)).

The time-averaged ACC transport is also strongly sensitive to resolution in both Smooth and Rough configurations. In particular, the transition from a smooth to rough bathymetry intensifies the ACC transport at eddy-permitting resolutions (increasing from 221.7 to 266.2 Sv at 20 km). In Section 4.3, the ACC transport will also be related to horizontal density gradients and the bottom velocity. With a maximum ACC transport of 266.2 Sv (20 km horizontal grid spacing, rough bathymetry) and a minimum of 147.7 Sv (40 km horizontal grid spacing, rough bathymetry), it is important to assess if such large variations in the ACC transport modify the Weddell Gyre transport directly.

4.2. ACC Sensitivity Results

In the ACC sensitivity experiments, the strength of the ACC is varied by modifying the height of the sill in the idealized Drake Passage. As shown in Table 2, these experiments use horizontal grid spacings between 80 and 10 km and all experiments have a rough bathymetry.

The results of the ACC sensitivity experiment are shown in Figure 8 where we can immediately see that the gyre transport barely responds (~1 Sv) to large changes in the idealized ACC transport (~100 Sv) at all tested resolutions. The large changes in the Weddell Gyre transport with resolution are controlled by the gyre's direct sensitivity to resolution and not the gyre's sensitivity to the ACC strength.

4.3. Thermal Wind and Bottom Flow Decomposition

In Section 4.1 we observe that the idealized Weddell Gyre and ACC transports are sensitive to horizontal resolution and are particularly strong at eddy-permitting resolutions. In this section, we relate the observed transports to the isopycnal structure of the circulation and the strength of the circulation at the sea floor. The depth-integrated velocity field is separated into depth-dependent and depth-independent components using integration by parts,

$$\mathbf{U} = \int_{-H}^{\eta} \mathbf{u} \, dz = \mathbf{u}_b H + \mathbf{u}_t \eta - \int_{-H}^{\eta} \frac{\partial \mathbf{u}}{\partial z} z \, dz, \quad (4)$$

where $\mathbf{U}$ is the depth-integrated velocity field, η is the free surface height, $\mathbf{u}_b$ is the velocity at the sea floor, and $\mathbf{u}_t$ is the velocity at the free surface. We then use the following equation to describe how the velocity field varies with depth,
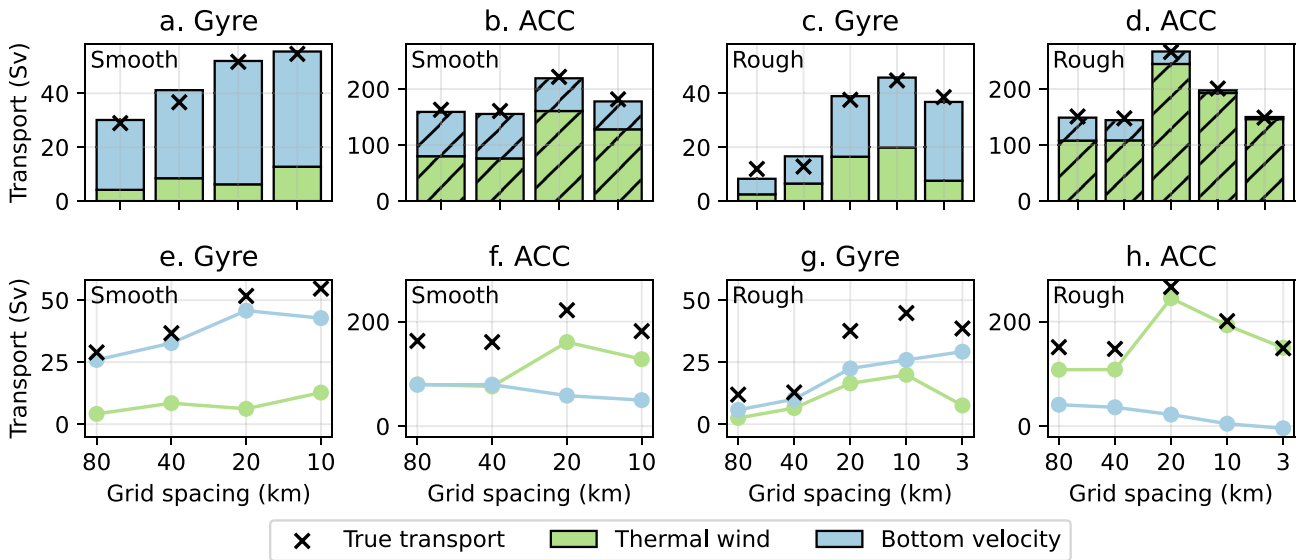
Figure 9. A decomposition of the gyre and Antarctic Circumpolar Current (ACC) transports over smooth and rough bathymetries. The thermal wind component describes the geostrophic transport which emerges from horizontal density gradients. The bottom velocity component describes the depth-independent transport which is determined by the velocity at the sea floor ($u_b H$). The black crosses mark the total gyre and ACC transports shown in Figure 7.

$$f \frac{\partial \mathbf{u}}{\partial z} = -\frac{g}{\rho_0}\left(\hat{\mathbf{k}} \times \boldsymbol{\nabla}_h \rho\right) + \boldsymbol{\mathcal{E}}, \tag{5}$$

where g is the acceleration due to gravity, ρ_0 is the reference density, $\boldsymbol{\nabla}_h$ is the horizontal gradient operator, ρ is the density, and $\boldsymbol{\mathcal{E}}$ is a residual function. Equation 5 is the thermal wind equation where all non-geostrophic terms, non-hydrostatic terms, and numerical errors are aggregated in $\boldsymbol{\mathcal{E}}$. The model used in this article assumes hydrostatic balance so $\boldsymbol{\mathcal{E}}$ is free of non-hydrostatic terms.

By combining Equations 4 and 5 we can derive a full decomposition of the depth-integrated flow,

$$\mathbf{U} = \underbrace{\mathbf{u}_b}_{\text{Bottom velocity}} + \underbrace{\frac{g}{\rho_0 f}}_{\text{Thermal wind}} + \mathbf{u}_t \eta + \boldsymbol{\mathcal{E}}^z, \tag{6}$$

where $\boldsymbol{\mathcal{E}}^z$ is the depth-integrated and rescaled residual that still contains non-geostrophic terms and errors from the discretization. The free surface term, $\mathbf{u}_t \eta$, is negligible in all of the presented results.

Using Equation 6, we decompose the Weddell Gyre and ACC transport into depth-independent ($\mathbf{u}_b H$) and depth-dependent components (thermal wind and residual). The decomposed transports and the associated stream functions are shown in Figures 9 and 10 respectively. In order to calculate valid stream functions, a Helmholtz decomposition of each term in Equation 6 is determined using an elliptical solver and the divergent part is removed. The full circulation has a weak divergent component and when this component is removed the largest change in the stream function is 0.03 Sv. The full circulation is approximately incompressible, so only the incompressible components of the terms in Equation 6 influence the full circulation. Each component of the gyre transport shown in Figure 9 is equal to the component's stream function evaluated where the gyre's total transport is calculated (black crosses, Figure 10). This definition was chosen as it describes the decomposition of the quantity of interest, the gyre's transport. As shown in Figure 10, the maximum of a specific component's stream function in the gyre basin (blue crosses) does not necessarily align with the gyre center. The ACC transport components shown are the zonal averages, but zonal variations of the decomposition are small and do not alter our interpretation of the results.

In all cases, the combined transport from the bottom flow and thermal wind component closely describes the total transport of the gyre (black crosses in Figure 9). This suggests that the residual terms are minor when considering the gyre and ACC transports. The circulation associated with the residual term, $\boldsymbol{\mathcal{E}}^z$, is weak across
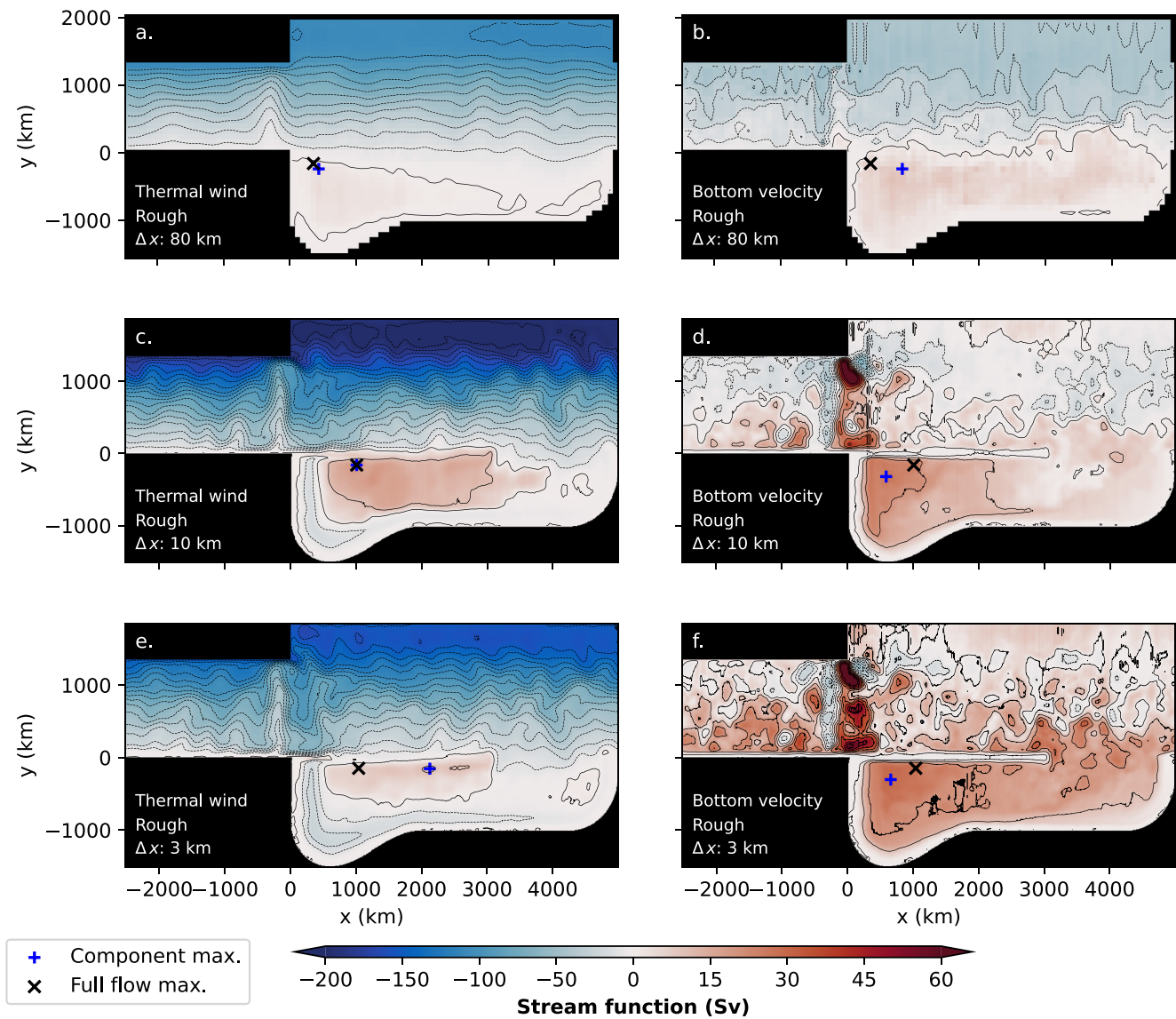
Figure 10. Stream functions from the same decomposition shown in Figure 9 at various resolutions. The black contours have an interval of 10 Sv. Results are from configurations with a rough bathymetry. The combined thermal wind and bottom velocity stream function is approximately equal to the total stream function, shown in Figure 7. Blue crosses mark the location of the component stream function maximum in the gyre basin. Black crosses mark the location where the total gyre transport is calculated.

most of the horizontal domain meaning that the depth-integrated circulation can be described to leading order using geostrophic assumptions. It is important to note that a small value of $\mathcal{E}^z$ does not guarantee geostrophy at all depths. The residual is largest at lower resolutions, this may be caused by small departures from geostrophy through viscous effects or a larger numerical error that comes with a coarser grid.

Looking at the gyre transports, the relative significance of the bottom velocity and the thermal wind component depends on the coarseness of the bathymetry. In the Smooth configurations, the bottom velocity plays a dominant role in controlling the gyre transport and increases with horizontal resolution. In configurations with a rough bathymetry, the gyre transport from the bottom flow is reduced and comparable to the thermal wind component, but still increases with resolution. When a rough bathymetry is used, the thermal wind component of the gyre is particularly strong with a 10 km horizontal grid spacing and consequently the total gyre transport is particularly strong at eddy-permitting resolutions.

The decomposition of the ACC transport is also dependent on the coarseness of the bathymetry. In simulations with a smooth bathymetry, contributions to the ACC transport from the bottom flow and thermal wind

components are similar in size (Figure 9b). The bottom flow component shrinks with resolution and the thermal wind component is largest at an eddy-permitting resolution (20 km in Figure 9b). When a rough bathymetry is used, the ACC transport is almost entirely determined by the thermal wind component, which is even larger at eddy-permitting resolutions (see Figure 9d). The decomposition of the ACC with rough bathymetry is more realistic as observations (Chidichimo et al., 2014; Donohue et al., 2016; Koenig et al., 2014) suggest that the ACC transport is largely determined by a thermal wind (or often called "baroclinic") component.

The shape of the stream function from the bottom flow and the thermal wind components differ. The thermal wind stream function (left column of Figure 10) features a gyre that lies over the basin interior and submarine ridge and is not west-intensified. Over the continental shelf there is a density-driven slope current that reverses direction south of the submarine ridge, which is a consequence of the idealized model design. An accurate slope current may require a wind stress that follows the continental shelf (Thompson et al., 2018). The stream function for the bottom flow transport (right column of Figure 10) features a gyre that follows the bathymetry closely and is west-intensified. The submarine ridge blocks the deep current but the bottom flow is free to extend northwards into the ACC channel once it is far enough east.

Over the submarine ridge the thermal wind and bottom velocity stream functions reinforce each other, resulting in a particularly strong western and northern boundary current. In contrast the thermal wind and bottom velocity stream function are opposite-signed on the continental shelf, which limits the gyre's presence over the continental shelf in all simulations. In higher resolution simulations, the bottom velocity stream functions uniquely feature intense recirculations to the east of the Drake Passage.

4.4. Sensitivity of the Thermal Wind Component to Resolution

In the previous section we note that the depth-varying component of the flow can be closely described by the thermal wind relation and ultimately related to horizontal density gradients. To understand why the thermal wind component of the gyre and the ACC is particularly strong at eddy-permitting resolutions, we study the isopycnal structure at various resolutions. Zonal averages of the density are calculated over five meridional sections: Channel ($-2,000 < x < -1,000$ km), West Ridge ($500 < x < 1,000$ km), East Ridge ($2,000 < x < 2,500$ km), East of the ridge ($3,500 < x < 4,000$ km), and the full zonal average. The locations of these sections are shown in Figure 6e.

Figure 11 compares the isopycnal structure between an eddy-permitting (10 km) and an eddy-parameterized (80 km) simulation with rough bathymetry. The isopycnal structure for simulations with a smooth bathymetry are qualitatively similar. In all meridional sections, the isopycnals are more tilted in the eddy-permitting simulation. In particular, meridional density gradients over the submarine ridge are large at eddy-permitting resolutions and the stratification of the gyre basin ($y < 0$) is reduced. At eddy-permitting and eddy-rich resolutions, the submarine ridge plays a large role in setting the nearby stratification; this is in agreement with observations (such as Figure 1b) and the findings of Wilson et al. (2022). From Figure 11 we can conclude that the thermal wind component of the gyre and ACC transports is larger in eddy-permitting models as density gradients are more extreme in the upper 2,000 m of the model. A thick and weakly stratified layer also emerges in the eddy-permitting simulations, which is approximately below the 1,028.5 kg m^{-3} contour. In this layer, horizontal density gradients are small and the thermal wind relation suggests that the zonal flow is not expected to vary significantly with depth.

Figure 12 compares the isopycnal structure between an eddy-rich (3 km) and the same eddy-permitting (10 km) simulation with rough bathymetry. The isopycnals of the eddy-rich and eddy-permitting simulations share similar features, however meridional density gradients are smaller in the eddy-rich case. This is particularly noticeable above the submarine ridge and ultimately reduces the thermal wind transport of the gyre and ACC in the upper 2,000 m of the model. The reduced outcropping of isopycnals in the eddy-rich model also increases the stratification of the gyre basin and reduces the thickness of the weakly stratified layer (approximately below 1,028.5 kg m^{-3} contour). In simulations with explicit eddies, the densest isopycnals ourcrop approximately 200 km south of the submarine ridge. In this area, the wind stress curl is at its peak negative value and there is little buoyancy forcing (see Figures 2c and 2d). It is therefore possible that there is an Ekman control on the maximum surface density in the gyre basin.

Such large horizontal density gradients are uncommon in eddy-parameterized models. The eddy-parameterized models (80 and 40 km) include the strongest tracer diffusion terms and eddy schemes like the GM parameterization simulate the effect of unresolved eddies by flattening isopycnals. In the presented simulations (and many
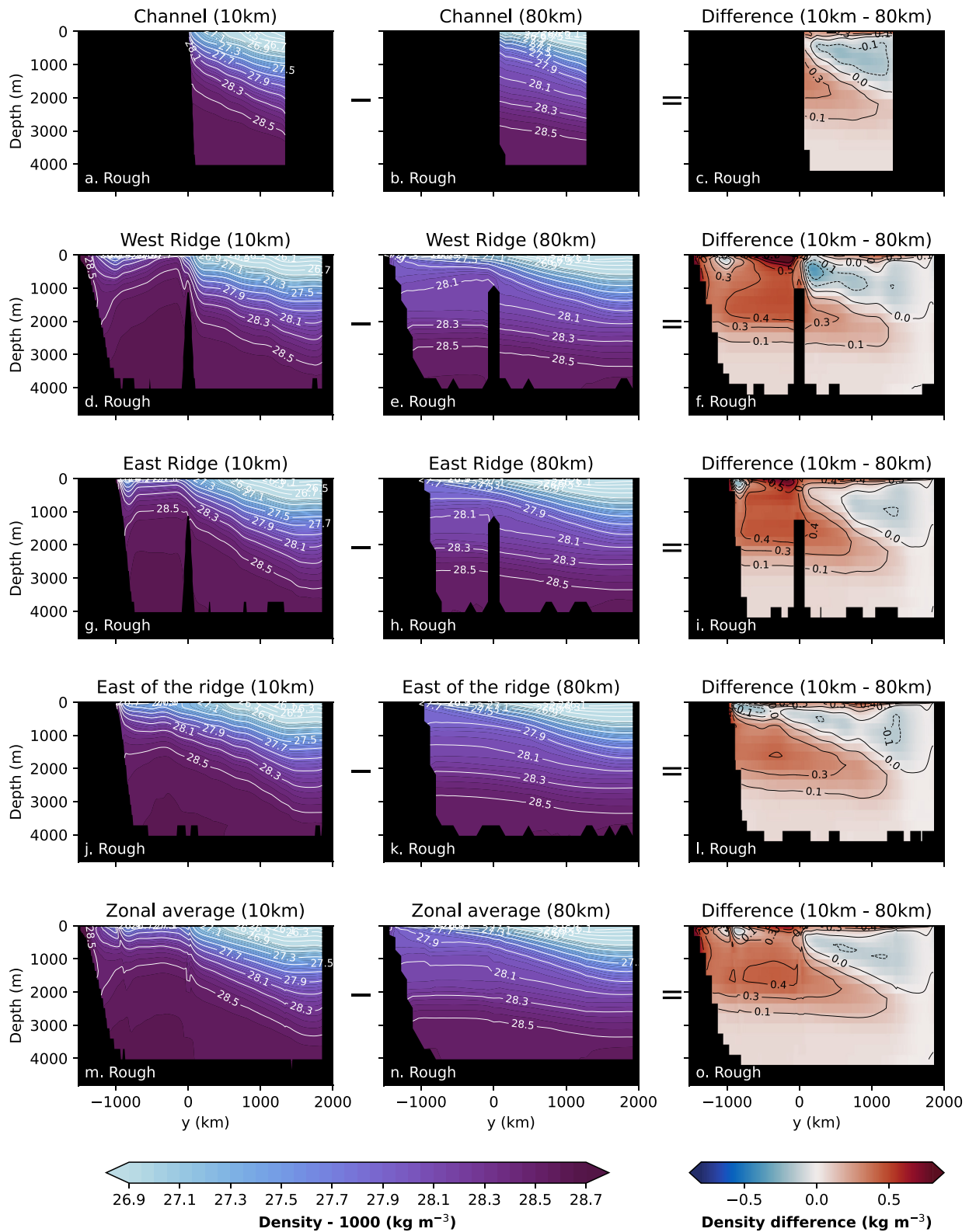
Figure 11. Meridional density sections of an eddy-permitting (10 km, left column) and an eddy parameterized (80 km, middle column) simulation. The difference between the density sections are shown in the right column. All presented sections feature a rough bathymetry.
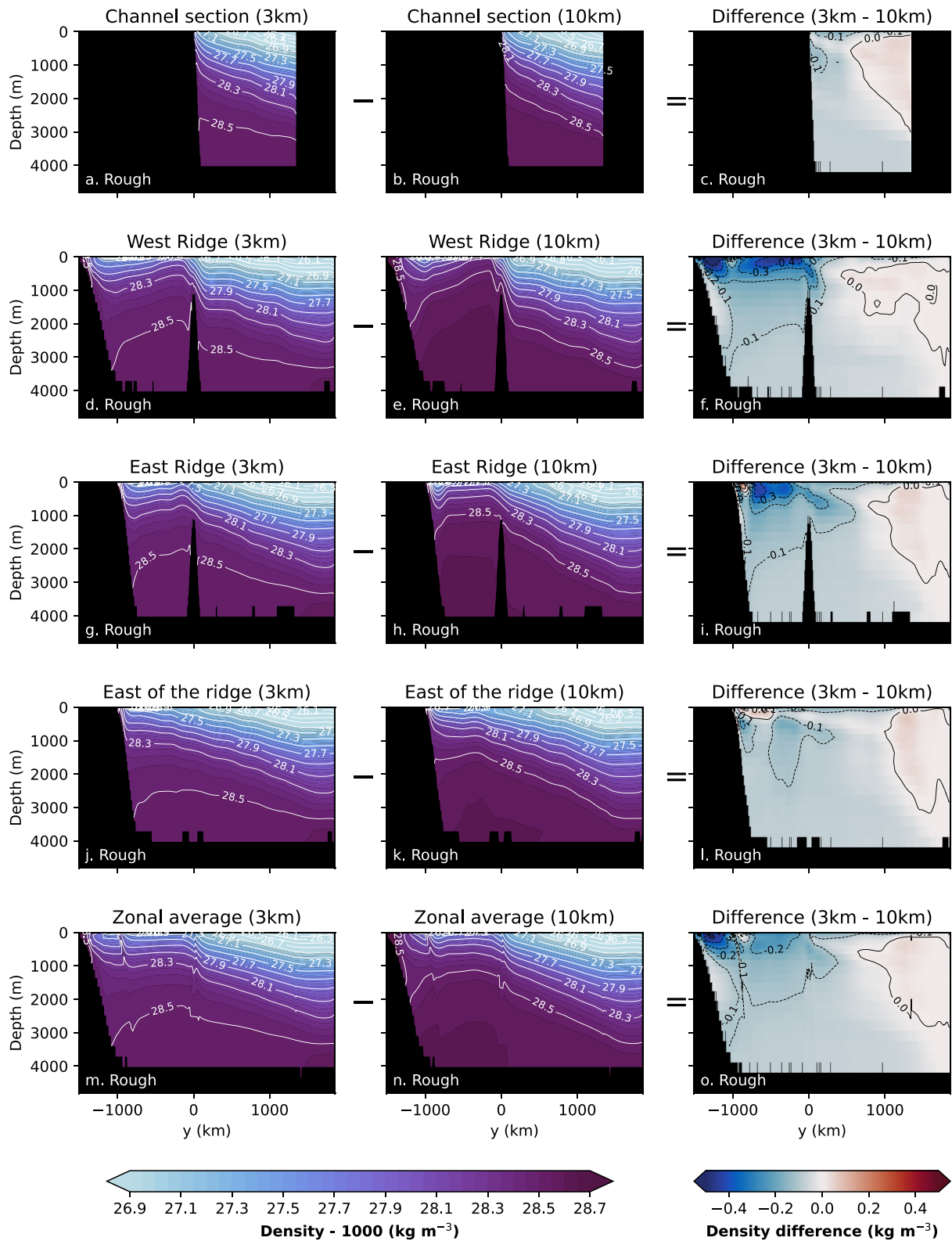
Figure 12. Meridional density sections of an eddy-rich (3 km, left column) and an eddy-permitting (10 km, middle column) simulation. The difference between the density sections are shown in the right column. All presented sections feature a rough bathymetry.
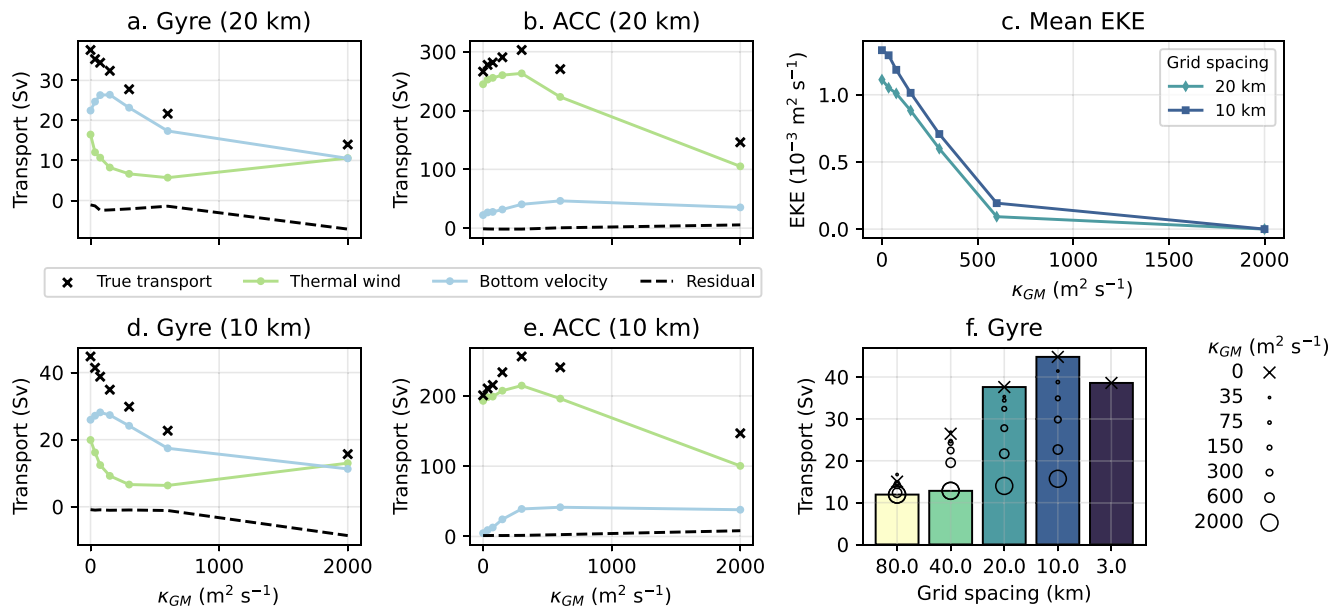
Figure 13. The effect of using GM in eddy-permitting models. (a, d) Show the transport of the Weddell Gyre with applications of GM at various strengths alongside the thermal wind decomposition. (b, e) Show the transport of the Antarctic Circumpolar Current with applications of GM at various strengths alongside the thermal wind decomposition. (c) Is the mean eddy kinetic energy when the GM diffusivity parameter is varied. (f) Compares the various gyre transports when GM is applied to the transports shown in Figure 7c. The strength of GM is similarly varied in the eddy-parameterized models and the effect on the gyre transport is shown in (f).

climate models), the diffusion parameters and the parameterized eddies are insensitive to topographic features and consequently the isopycnals are relatively flat over the submarine ridge and the gyre basin. In reality, eddy diffusivity can be significantly reduced over large topographic features (Isachsen, 2011). This effect can be seen in our eddy-rich simulation as well; in Figure 6c, the eddy kinetic energy reduces by an order of magnitude above the submarine ridge and the continental shelf.

The eddy-permitting simulations are significantly less diffusive and no eddy-parameterization is used. The partially resolved eddy field is insufficient to flatten the isopycnals to the same extent as the eddy-parameterized models and therefore more extreme density gradients emerge. In the eddy-rich simulation (3 km), diffusive terms are small, but the near-resolved mesoscale eddy field is able to flatten the density surfaces more effectively than the partially-resolved eddy field. In Section 4.5, we test if various applications of GM in eddy-permitting models can change our results.

4.5. Using GM at Eddy-Permitting Resolutions

In the results shown so far, all eddy-permitting simulations do not use the GM parameterization. In this subsection we investigate how strong to weak applications of GM affect our gyre and ACC transports at eddy-permitting resolutions. In simulations with 10 and 20 km horizontal grid spacings and rough bathymetry, the GM diffusivity parameter was varied from 35 m^2 s^{-1} up to 2,000 m^2 s^{-1} (the value used in lower resolution simulations). The results of this sensitivity experiment are shown in Figure 13.

At both eddy-permitting resolutions (Figures 13a and 13d), the gyre transport decreases as the strength of the GM parameterization increases. Up until the strongest application of GM, the thermal wind component of the gyre transport weakens, suggesting the density surfaces are flattening in response to the increased GM diffusivity. When the GM diffusivity equals 2,000 m^2 s^{-1}, the residual of the thermal wind decomposition is significant, making it difficult to assess the relative importance of the thermal wind transport. The general weakening of the gyre transport is accompanied by a reduction in the overall eddy kinetic energy of the model (Figure 13c).

Figure 13f contextualizes these eddy-permitting results. We find that weak applications of GM (75 m^2 s^{-1} or less) in eddy-permitting models can improve their agreement with eddy-rich models at the expense of some explicit eddy kinetic energy. Stronger applications of GM (600 m^2 s^{-1} or more) in eddy-permitting models can improve

their agreement with the eddy-paramaterized models but reduces the explicit mean eddy kinetic energy by an order of magnitude. In Figure 13f, the gyre transport still slowly increases with resolution when a GM diffusivity of 2,000 $m^2 s^{-1}$ is used. In the absence of explicit eddies, this slow increase is likely a result of increased resolution of the mean flow, increased resolution of the bathymetry, or the linear variation of the momentum and tracer diffusivity with horizontal grid spacing.

For completeness, we also shown in Figure 13f what happens to the gyre transport when the GM parameter is similarly varied in eddy-parameterized models. In the 80 km case, the gyre transport was insensitive to variations in the GM parameter and has a maximum value of 16.7 Sv when the GM parameter is 35 $m^2 s^{-1}$. In the 40 km case, the gyre transport is more sensitive to the variation in the GM parameter and has a maximum value of 26.8 Sv when the GM paramater is 35 $m^2 s^{-1}$. Significantly reducing the strength of GM in eddy-parameterized models (from 2,000–75 $m^2 s^{-1}$ or less) can increase the gyre transport but does not lead to agreement with the eddy-rich simulations.

Figure 13f shows that in our experiment, no selection of GM diffusivities can produce a consistent gyre transport between all horizontal resolutions. Using different applications of GM (e.g., spatially varying diffusivities) and alternative parameterizations may yield different results. Exploring these approaches with the model would be a valuable contribution to the ocean modeling community but is beyond the scope of the present study.

5. Discussion

In the previous section, we related the thermal wind component of the gyre and ACC transports to the density structure. In contrast, it is not immediately clear why the transport from the bottom flow can vary significantly with resolution. To explore this sensitivity of the bottom flow to resolution, we discuss the potential contributions of non-linear eddy-mean flow interactions. We will then discuss other physical processes that are neglected in our idealized model.

5.1. Role of Eddies

In this article, we observe that the density surfaces of the idealized Weddell Gyre change significantly when explicit eddies are introduced to ocean simulations and that the density structure has a significant influence on the horizontal circulation. In the presence of rough bathymetry, the thermal wind component of the gyre transport intensifies in simulations with explicit eddies because the meridional density gradients are steeper. In Figure 6, we see large eddy kinetic energies in areas where the isopycnal tilt is the most extreme. This suggests that the increase in the mean available potential energy that comes with steeper isopycnals can fuel more energetic mesoscale eddies.

A component of the mesoscale eddy field extends to the sea floor, as shown by the vertical bands of eddy kinetic energy in Figure 6. It therefore seems likely that explicit mesoscale eddies are influencing the bottom flow in select areas of the model (e.g., between 1,000 and 500 km south of the submarine ridge in Figure 6b). In the presence of variable bottom topography, mesoscale eddies can drive a mean circulation along topographic contours (Bretherton & Haidvogel, 1976). This can be interpreted either as an "entropic force" (Holloway, 1987, 1992) or, alternatively, as energetically constrained mixing of potential vorticity over the sloping topography (Adcock & Marshall, 2000; Bretherton & Haidvogel, 1976). In Stewart et al. (2019), a simulated Antarctic Slope Current is partially accelerated by mesoscale eddy vorticity fluxes. These eddy-driven flows are not captured by eddy parameterizations employed in climate models based on GM. However, it is possible that these entropic forces are captured in our simulations with explicit eddies, consistent with the strengthening of the bottom flow at higher resolutions. This deserves further investigation, but is beyond the scope of the present study.

As eddy-permitting models become more feasible for climate projections, there is an increasing interest in developing eddy parameterizations for simulations where the largest eddies are at least marginally resolved. The development and testing of eddy parameterizations is a busy area of research; Hewitt et al. (2020) review the various approaches that could be deployed in eddy-parameterized and eddy-permitting ocean models. Of particular relevance to the Weddell Gyre is a recent study by Wei et al. (2022) which finds encouraging results for parameterized mesoscale eddy buoyancy fluxes over large scale bathymetry when topographic suppression effects are incorporated.

5.2. Missing Physics in the Idealized Configuration

Before concluding on the results presented in this article, it is important to summarize the limitations of the idealized model. First, the winds in these configurations are zonal and do not follow the continental shelf. This may be the reason why the density driven slope current in this model does not reach the Drake Passage; additionally, a complete slope current may require deep passages in the zonal submarine ridge. In Figure 12, the isopycnals tilt upwards when above the continental shelf. This suggests that dense water is being exported everywhere along the shelf. In reality, dense water export is more localized and isopycnals would tilt down above the continental shelf in East Antarctica (Thompson et al., 2018). Non-linearities in the equation of state may also be important for AABW formation (Gill & Niller, 1973), so using a linear equation of state may lead to inaccurate densities. Presently, it is unclear if a more accurate slope current would modify the gyre transport significantly.

We imitate the time-averaged effect of ice with an effective freshwater flux shown in Figure 2d but no attempt is made to couple the effect of sea ice to the oceanic or atmospheric state. In addition, the effect of internal stresses in the ice can modify the surface stress experienced by the ocean. By neglecting internal stresses, we are assuming that all ice is in "free drift" which may not be valid near the continental shelf according to satellite observations (Kimura, 2004; Kwok et al., 2017). In reality, the Weddell Gyre and ACC are exposed to an extreme seasonal cycle which significantly varies the gyre's transport (Neme et al., 2021) and density structure on the western boundary (Hattermann, 2018). The seasonal variability of the wind stress and buoyancy forcing can be larger than the time-averaged forcing. In this work we are assuming that time-averaged forcing will accurately produce a time-averaged Weddell Gyre and ACC, but this may not be true because of non-linear processes. This is certainly not true for the subpolar gyres in the northern hemisphere, where winter conditions play a disproportionately large role in setting the properties of the deep ocean thermocline as waters subducted at any time outside of late-winter are re-entrained by the dynamic mixed layer (Stommel, 1979). A similar mechanism also operates on an inter-annual time scale in the northern hemisphere (MacGilchrist et al., 2021). It is unclear if a similar selection process ("Stommel's Demon") is present in the Southern Ocean and needs further investigation. All experiments used in this study are in a statistically steady state (see Figure 4), unlike the real ocean which is exposed to an extreme seasonal cycle, a changing global ocean, and a changing climate.

The large-scale topographic features in the model (shown in Figure 2a) are qualitatively similar to the Weddell basin but there are some important differences. First, the submarine ridge and the northern boundary of the domain are zonal. The meridional components of the idealized Weddell Gyre and ACC are too constrained by bottom topography when compared to the real ocean. In reality, the ACC is deflected northwards immediately upon exiting the Drake Passage (Mazloff et al., 2010) which is a behavior this idealized model cannot recreate as any northward deflection of the ACC is limited by the sponge region. Finally, a unique feature of the Weddell Gyre is its dynamic shape as no obvious topographic feature constrains the gyre's eastern boundary (Vernet et al., 2019). In our idealized simulations, the zonal extent of the Weddell Gyre is not able to extend beyond the width of the basin (5,000 km) without taking a northward departure into the ACC channel.

6. Conclusions

Using a minimal description of the Weddell Gyre and ACC, we have identified an extreme sensitivity of the circulation to horizontal grid spacing between eddy-parameterized and eddy-permitting resolutions. The Weddell Gyre in eddy-permitting simulations is significantly stronger than in eddy-parameterized cases and slightly stronger than an eddy-rich case (Figure 7). This is concerning as coupled climate models are beginning to traverse this highly sensitive "gray zone," where large mesoscale eddies are only partially resolved.

To investigate if the gyre transports are affected by the varying ACC strength, we performed a sensitivity experiment in Section 4.2. The channel topography was modified to either increase or decrease the ACC transport at eddy-parameterized and eddy-permitting resolutions and the effect on the Weddell Gyre was negligible (Figure 8). The limited coupling of the gyre and ACC transports was useful for our study but the insensitivity itself is also scientifically interesting and should be investigated further.

To improve our understanding of the flow's vertical structure, we used a thermal wind decomposition in Section 4.3 which works well with a small residual (Figure 9). In cases with a smooth bathymetry, the gyre strength is almost entirely determined by the depth-independent, bottom flow transport, $\mathbf{u}_b H$. When a rough bathymetry is used, the bottom gyre transport is comparable in size to the thermal wind transport, which varies with depth. Although the

total transport sensitivity to resolution is similar with smooth and rough bathymetry, the vertical and horizontal structure of the flow clearly differs. This highlights how permitting small topographic interactions everywhere in an idealized model can change large scale circulation features.

With a rough bathymetry, the thermal wind component of the gyre is particularly large over the submarine ridge (Figures 11 and 12). This is a behavior which was found in the work of Wilson et al. (2022) and in hydrographic sections (such as Figure 1b). Wilson et al. (2022) found that the submarine ridge plays a fundamental role in setting the stratification and circulation of the Weddell Gyre and the ACC. This result holds true in our experiments at eddy-permitting and eddy-rich resolutions. However, we would need to study simulations without the submarine ridge to fully assess its impact on the gyre at various resolutions.

The thermal wind component of the gyre is largest at eddy-permitting resolutions because the partially-resolved eddy field is less effective at flattening isopycnals than a fully-resolved eddy field or an eddy parameterization. In all cases, the bottom flow transport of the gyre increases significantly when explicit eddies are present. In Section 4.5, we showed that using a weak application of the GM parameterization can bring eddy-permitting gyre transports down to eddy-rich values at the expense of some explicit eddy kinetic energy (Figure 13). Only a strong application of GM can significantly reduce the gyre's extreme sensitivity to horizontal resolution between eddy-parameterized and eddy-permitting scales and this would be at the expense of practically all explicit eddy kinetic energy. We also varied the strength of GM in the eddy-parameterized models and found that judicious choices of the GM parameter can minimize the gyre transport's sensitivity to resolution. However, no selection of GM parameters can avoid a factor of 3–4 difference in the gyre transport between the coarsest and finest resolutions.

In this study, the Weddell Gyre transport is largest and the isopycnals are the steepest at eddy-permitting resolutions. For this reason, ocean modelers should approach this eddy-permitting "gray zone" with care when simulating the Southern Ocean and consider employing parameterizations that are compatible with partially resolved mesoscale eddies.

Appendix A: Computational Cost of the Experiments

In this section, we summarize the computational cost of running the idealized model at various resolutions. On ARCHER2 the 20 km model required 1.2 node hours per model year; the 10 km model required 6.1 node hours per model year; and the 3 km model required 154.0 node hours per model year. On Monsoon2, the 80 km model required 0.4 node hours per model year and the 40 km model required 0.1 node hours per model year. The 80 km model has 132,525 grid points; the 40 km model has 509,733 grid points; the 20 km model has 1,998,477 grid points; the 10 km model has 7,889,934 grid points; and the 3 km model has 87,077,760 grid points.

Data Availability Statement

Input files for the idealized model integrations are archived on Zenodo (Styles et al., 2023b). The idealized configuration, designed for NEMO release 4.0.1, is available on Zenodo (Styles et al., 2023c). The software used to analyze the model outputs is also archived on Zenodo (Styles et al., 2023a).

References

Abernathey, R. P., Cerovecki, I., Holland, P. R., Newsom, E., Mazloff, M., & Talley, L. D. (2016). Water-mass transformation by sea ice in the upper branch of the Southern Ocean overturning. *Nature Geoscience*, *9*(8), 596–601. https://doi.org/10.1038/ngeo2749

Adcock, S. T., & Marshall, D. P. (2000). Interactions between geostrophic eddies and the mean circulation over large-scale bottom topography. *Journal of Physical Oceanography*, *30*(12), 3223–3238. https://doi.org/10.1175/1520-0485(2000)030⟨3223:IBGEAT⟩2.0.CO;2

Adcroft, A., Anderson, W., Balaji, V., Blanton, C., Bushuk, M., Dufour, C. O., et al. (2019). The GFDL Global Ocean and Sea Ice Model OM4.0: Model description and simulation features. *Journal of Advances in Modeling Earth Systems*, *11*(10), 3167–3211. https://doi.org/10.1029/2019MS001726

Argo. (2020). Argo float data and metadata from Global Data Assembly Centre (Argo GDAC). https://doi.org/10.17882/42182

Armitage, T. W. K., Kwok, R., Thompson, A. F., & Cunningham, G. (2018). Dynamic topography and sea level anomalies of the Southern Ocean: Variability and teleconnections. *Journal of Geophysical Research: Oceans*, *123*(1), 613–630. https://doi.org/10.1002/2017JC013534

Bougeault, P., & Lacarrere, P. (1989). Parameterization of orography-induced turbulence in a mesobeta–scale model. *Monthly Weather Review*, *117*(8), 1872–1890. https://doi.org/10.1175/1520-0493(1989)117⟨1872:POOITI⟩2.0.CO;2

Bretherton, F. P., & Haidvogel, D. B. (1976). Two-dimensional turbulence above topography. *Journal of Fluid Mechanics*, *78*(1), 129–154. https://doi.org/10.1017/S002211207600236X

Chidichimo, M. P., Donohue, K. A., Watts, D. R., & Tracey, K. L. (2014). Baroclinic transport time series of the Antarctic Circumpolar Current measured in Drake Passage. *Journal of Physical Oceanography*, *44*(7), 1829–1853. https://doi.org/10.1175/JPO-D-13-071.1

Deacon, G. E. R. (1979). The Weddell Gyre. *Deep Sea Research Part A: Oceanographic Research Papers*, *26*(9), 981–995. https://doi.org/10.1016/0198-0149(79)90044-X

Donohue, K. A., Tracey, K. L., Watts, D. R., Chidichimo, M. P., & Chereskin, T. K. (2016). Mean Antarctic Circumpolar Current transport measured in Drake Passage. *Geophysical Research Letters*, *43*(22), 11760–11767. https://doi.org/10.1002/2016GL070319

Fahrbach, E., Knoche, M., & Rohardt, G. (1991). An estimate of water mass transformation in the southern Weddell Sea. *Marine Chemistry*, *35*(1–4), 25–44. https://doi.org/10.1016/S0304-4203(09)90006-8

Fox-Kemper, B. (2018). Notions for the motions of the oceans. In E. P. Chassignet, A. Pascual, J. Tintoré, & J. Verron (Eds.), *New frontiers in operational oceanography*. GODAE OceanView. https://doi.org/10.17125/gov2018.ch02

Gaspar, P., Grégoris, Y., & Lefevre, J.-M. (1990). A simple eddy kinetic energy model for simulations of the oceanic vertical mixing: Tests at station Papa and long-term upper ocean study site. *Journal of Geophysical Research*, *95*(C9), 16179–16193. https://doi.org/10.1029/JC095iC09p16179

Gent, P. R., & McWilliams, J. C. (1990). Isopycnal mixing in ocean circulation models. *Journal of Physical Oceanography*, *20*(1), 150–155. https://doi.org/10.1175/1520-0485(1990)020⟨0150:imiocm⟩2.0.co;2

Gill, A. E., & Niller, P. P. (1973). The theory of the seasonal variability in the ocean. *Deep Sea Research and Oceanographic Abstracts*, *20*(2), 141–177. https://doi.org/10.1016/0011-7471(73)90049-1

Gordon, A. L., Martinson, D. G., & Taylor, H. W. (1981). The wind-driven circulation in the Weddell-Enderby Basin. *Deep Sea Research Part A: Oceanographic Research Papers*, *28*(2), 151–163. https://doi.org/10.1016/0198-0149(81)90087-X

Haid, V., & Timmermann, R. (2013). Simulated heat flux and sea ice production at coastal polynyas in the southwestern Weddell Sea. *Journal of Geophysical Research: Oceans*, *118*(5), 2640–2652. https://doi.org/10.1002/jgrc.20133

Hallberg, R. (2013). Using a resolution function to regulate parameterizations of oceanic mesoscale eddy effects. *Ocean Modelling*, *72*, 92–103. https://doi.org/10.1016/j.ocemod.2013.08.007

Hattermann, T. (2018). Antarctic thermocline dynamics along a narrow shelf with easterly winds. *Journal of Physical Oceanography*, *48*(10), 2419–2443. https://doi.org/10.1175/JPO-D-18-0064.1

Hewitt, H. T., Roberts, M., Mathiot, P., Biastoch, A., Blockley, E., Chassignet, E. P., et al. (2020). Resolving and parameterising the ocean mesoscale in earth system models. *Current Climate Change Reports*, *6*(4), 137–152. https://doi.org/10.1007/s40641-020-00164-w

Holloway, G. (1987). Systematic forcing of large-scale geophysical flows by eddy-topography interaction. *Journal of Fluid Mechanics*, *184*, 463–476. https://doi.org/10.1017/S0022112087002970

Holloway, G. (1992). Representing topographic stress for large-scale ocean models. *Journal of Physical Oceanography*, *22*(9), 1033–1046. https://doi.org/10.1175/1520-0485(1992)022⟨1033:RTSFLS⟩2.0.CO;2

Isachsen, P. E. (2011). Baroclinic instability and eddy tracer transport across sloping bottom topography: How well does a modified Eady model do in primitive equation simulations? *Ocean Modelling*, *39*(1), 183–199. https://doi.org/10.1016/j.ocemod.2010.09.007

Katsumata, K., Purkey, S. G., Cowley, R., Sloyan, B. M., Diggs, S. C., Moore, T. S., et al. (2022). GO-SHIP Easy Ocean: Gridded ship-based hydrographic section of temperature, salinity, and dissolved oxygen. *Scientific Data*, *9*(1), 103. https://doi.org/10.1038/s41597-022-01212-w

Kimura, N. (2004). Sea ice motion in response to surface wind and ocean current in the Southern Ocean. *Journal of the Meteorological Society of Japan. Series II*, *82*(4), 1223–1231. https://doi.org/10.2151/JMSJ.2004.1223

Kiss, A. E., Hogg, A. M., Hannah, N., Boeira Dias, F., Brassington, G. B., Chamberlain, M. A., et al. (2020). ACCESS-OM2 v1.0: A global ocean–sea ice model at three resolutions. *Geoscientific Model Development*, *13*(2), 401–442. https://doi.org/10.5194/gmd-13-401-2020

Koenig, Z., Provost, C., Ferrari, R., Sennéchael, N., & Rio, M.-H. (2014). Volume transport of the Antarctic Circumpolar Current: Production and validation of a 20 year long time series obtained from in situ and satellite observations. *Journal of Geophysical Research: Oceans*, *119*(8), 5407–5433. https://doi.org/10.1002/2014JC009966

Kwok, R., Pang, S. S., & Kacimi, S. (2017). Sea ice drift in the Southern Ocean: Regional patterns, variability, and trends. *Elementa*, *5*, 32. https://doi.org/10.1525/ELEMENTA.226/112431

Lévy, M., Jahn, O., Dutkiewicz, S., Follows, M. J., & D'Ovidio, F. (2015). The dynamical landscape of marine phytoplankton diversity. *Journal of the Royal Society Interface*, *12*(111), 20150481. https://doi.org/10.1098/rsif.2015.0481

Lévy, M., Klein, P., Tréguier, A. M., Iovino, D., Madec, G., Masson, S., & Takahashi, K. (2010). Modifications of gyre circulation by sub-mesoscale physics. *Ocean Modelling*, *34*(1–2), 1–15. https://doi.org/10.1016/j.ocemod.2010.04.001

Lumpkin, R., & Speer, K. (2007). Global Ocean meridional overturning. *Journal of Physical Oceanography*, *37*(10), 2550–2562. https://doi.org/10.1175/JPO3130.1

MacGilchrist, G. A., Johnson, H. L., Lique, C., & Marshall, D. P. (2021). Demons in the North Atlantic: Variability of deep ocean ventilation. *Geophysical Research Letters*, *48*(9), 1–9. https://doi.org/10.1029/2020GL092340

Madec, G., Bourdallé-Badie, R., Chanut, J., Samson, E. C., Coward, A., Ethé, C., et al. (2019). NEMO ocean engine. *Zenodo*. https://doi.org/10.5281/zenodo.1464816

Madec, G., & Imbard, M. (1996). A global ocean mesh to overcome the North Pole singularity. *Climate Dynamics*, *12*(6), 381–388. https://doi.org/10.1007/BF00211684

Marshall, D. P., Ambaum, M. H., Maddison, J. R., Munday, D. R., & Novak, L. (2017). Eddy saturation and frictional control of the Antarctic Circumpolar Current. *Geophysical Research Letters*, *44*(1), 286–292. https://doi.org/10.1002/2016GL071702

Marshall, J., & Speer, K. (2012). Closure of the meridional overturning circulation through Southern Ocean upwelling. *Nature Geoscience*, *5*(3), 171–180. https://doi.org/10.1038/ngeo1391

Mazloff, M. R., Heimbach, P., & Wunsch, C. (2010). An eddy-permitting Southern Ocean state estimate. *Journal of Physical Oceanography*, *40*(5), 880–899. https://doi.org/10.1175/2009JPO4236.1

Meijers, A. J., Meredith, M. P., Abrahamsen, E. P., Morales Maqueda, M. A., Jones, D. C., & Naveira Garabato, A. C. (2016). Wind-driven export of Weddell Sea slope water. *Journal of Geophysical Research: Oceans*, *121*(10), 7530–7546. https://doi.org/10.1002/2016JC011757

Naveira Garabato, A. C., Zika, J. D., Jullion, L., Brown, P. J., Holland, P. R., Meredith, M. P., & Bacon, S. (2016). The thermodynamic balance of the Weddell Gyre. *Geophysical Research Letters*, *43*(1), 317–325. https://doi.org/10.1002/2015GL066658

Neme, J., England, M. H., & Hogg, A. M. C. (2021). Seasonal and interannual variability of the Weddell Gyre from a high-resolution global ocean-sea ice simulation during 1958–2018. *Journal of Geophysical Research: Oceans*, *126*(11), 1–19. https://doi.org/10.1029/2021JC017662

Orsi, A. H., Nowlin, W. D., & Whitworth, T. (1993). On the circulation and stratification of the Weddell Gyre. *Deep Sea Research Part I: Oceanographic Research Papers*, *40*(1), 169–203. https://doi.org/10.1016/0967-0637(93)90060-G

Orsi, A. H., Whitworth, T., & Nowlin, W. D. (1995). On the meridional extent and fronts of the Antarctic Circumpolar Current. *Deep Sea Research Part I: Oceanographic Research Papers*, *42*(5), 641–673. https://doi.org/10.1016/0967-0637(95)00021-W

Park, Y.-H., Charriaud, E., Craneguy, P., & Kartavtseff, A. (2001). Fronts, transport, and Weddell Gyre at 30°E between Africa and Antarctica. *Journal of Geophysical Research*, *106*(C2), 2857–2879. https://doi.org/10.1029/2000JC900087

Pellichero, V., Sallée, J. B., Chapman, C. C., & Downes, S. M. (2018). The southern ocean meridional overturning in the sea-ice sector is driven by freshwater fluxes. *Nature Communications*, *9*(1), 1–9. https://doi.org/10.1038/s41467-018-04101-2

Perezhogin, P. (2019). Deterministic and stochastic parameterizations of kinetic energy backscatter in the NEMO ocean model in Double-Gyre configuration. In *IOP conference series: Earth and environmental science*. https://doi.org/10.1088/1755-1315/386/1/012025

Reeve, K. A., Boebel, O., Strass, V., Kanzow, T., & Gerdes, R. (2019). Horizontal circulation and volume transports in the Weddell Gyre derived from Argo float data. *Progress in Oceanography*, *175*(August 2017), 263–283. https://doi.org/10.1016/j.pocean.2019.04.006

Ruggiero, G. A., Ourmières, Y., Cosme, E., Blum, J., Auroux, D., & Verron, J. (2015). Data assimilation experiments using diffusive back-and-forth nudging for the NEMO ocean model. *Nonlinear Processes in Geophysics*, *22*(2), 233–248. https://doi.org/10.5194/npg-22-233-2015

Ryan, S., Schröder, M., Huhn, O., & Timmermann, R. (2016). On the warm inflow at the eastern boundary of the Weddell Gyre. *Deep Sea Research Part I: Oceanographic Research Papers*, *107*, 70–81. https://doi.org/10.1016/j.dsr.2015.11.002

Schröder, M., & Fahrbach, E. (1999). On the structure and the transport of the eastern Weddell Gyre. *Deep Sea Research Part II: Topical Studies in Oceanography*, *46*(1), 501–527. https://doi.org/10.1016/S0967-0645(98)00112-X

Sloyan, B. M., & Rintoul, S. R. (2001). The Southern Ocean limb of the global deep overturning circulation. *Journal of Physical Oceanography*, *31*(1), 143–173. https://doi.org/10.1175/1520-0485(2001)031⟨0143:TSOLOT⟩2.0.CO;2

Spencer, K. (2022). OpenSimplex noise [Software]. GitHub. Retrieved from https://github.com/lmas/opensimplex

Stewart, A. L., Klocker, A., & Menemenlis, D. (2019). Acceleration and overturning of the Antarctic Slope Current by winds, eddies, and tides. *Journal of Physical Oceanography*, *49*(8), 2043–2074. https://doi.org/10.1175/JPO-D-18-0221.1

Stommel, H. (1979). Determination of water mass properties of water pumped down from the Ekman layer to the geostrophic flow below. *Proceedings of the National Academy of Sciences*, *76*(7), 3051–3055. https://doi.org/10.1073/pnas.76.7.3051

Styles, A. F., Bell, M. J., & Marshall, D. P. (2023a). Analysis software for "The sensitivity of an idealized Weddell Gyre to horizontal resolution" [Software]. Zenodo. https://doi.org/10.5281/zenodo.7969645

Styles, A. F., Bell, M. J., & Marshall, D. P. (2023b). Data for "The sensitivity of an idealized Weddell Gyre to horizontal resolution". *Zenodo*. https://doi.org/10.5281/zenodo.8392810

Styles, A. F., Bell, M. J., & Marshall, D. P. (2023c). Model configuration for "The sensitivity of an idealized Weddell Gyre to horizontal resolution" [Software]. Zenodo. https://doi.org/10.5281/zenodo.7969659

Styles, A. F., Bell, M. J., Marshall, D. P., & Storkey, D. (2022). Spurious forces can dominate the vorticity budget of ocean gyres on the C-grid. *Journal of Advances in Modeling Earth Systems*, *14*(5), e2021MS002884. https://doi.org/10.1029/2021MS002884

Talley, L. D., Reid, J. L., & Robbins, P. E. (2003). Data-based meridional overturning streamfunctions for the global ocean. *Journal of Climate*, *16*(19), 3213–3226. https://doi.org/10.1175/1520-0442(2003)016⟨3213:DMOSFT⟩2.0.CO;2

Thompson, A. F., Stewart, A. L., Spence, P., & Heywood, K. J. (2018). The Antarctic Slope Current in a changing climate. *Reviews of Geophysics*, *56*(4), 741–770. https://doi.org/10.1029/2018RG000624

Vernet, M., Geibert, W., Hoppema, M., Brown, P. J., Haas, C., Hellmer, H. H., et al. (2019). The Weddell Gyre, Southern Ocean: Present knowledge and future challenges. *Reviews of Geophysics*, *57*(3), 623–708. https://doi.org/10.1029/2018RG000604

Wang, Z. (2013). On the response of Southern Hemisphere subpolar gyres to climate change in coupled climate models. *Journal of Geophysical Research: Oceans*, *118*(3), 1070–1086. https://doi.org/10.1002/jgrc.20111

Wei, H., Wang, Y., Stewart, A. L., & Mak, J. (2022). Scalings for eddy buoyancy fluxes across prograde shelf/slope fronts. *Journal of Advances in Modeling Earth Systems*, *14*(12), e2022MS003229. https://doi.org/10.1029/2022MS003229

Wilson, E. A., Thompson, A. F., Stewart, A. L., & Sun, S. (2022). Bathymetric control of subpolar gyres and the overturning circulation in the Southern Ocean. *Journal of Physical Oceanography*, *52*(2), 205–223. https://doi.org/10.1175/JPO-D-21-0136.1

Yaremchuk, M., Nechaev, D., Schroter, J., & Fahrbach, E. (1998). A dynamically consistent analysis of circulation and transports in the southwestern Weddell Sea. *Annales Geophysicae*, *16*(8), 1024–1038. https://doi.org/10.1007/s00585-998-1024-7